

# AKARI and Spinning Dust Emission

A look at microwave dust emission via the Infrared

Aaron Christopher Bell

November 19, 2017

# **1 Abstract**

2 The anomalous microwave emission (AME) still lacks a coherent explanation. electric dipole emission  
3 by rapidly rotating dust (“spinning dust”) and magnetic dipole emission by grains with magnetic in-  
4 clusions (“magnetic dust”) have emerged as potential explanations. We explore the scenario in which  
5 spinning polycyclic aromatic hydrocarbon molecules (PAHs) are the dominant carriers of the AME.  
6 We use data from the AKARI/Infrared Camera (IRC), due to its thorough PAH-band coverage, to  
7 compare AME (Planck Coll. astrophysical component separation product) with infrared dust emis-  
8 sion. The results and discussion contained here apply to an angular scale of approximately  $1^\circ$ . In  
9 general, our results support an AME-from-dust hypothesis. At  $1^\circ$  angular resolution, we do not find  
10 evidence that the AME is exclusively carried by PAHs. The correlation of far IR dust emission with  
11 AME appears to be the best predictor, with MIR/PAH emission being marginally more weakly corre-  
12 lated with AME. In the case of lambda Orionis, AME vs. PAH is at least as strong as AME vs. FIR.  
13 Higher resolution studies will be needed in the future to fully solve the AME mystery. re consistent  
14 with previous studies in that the AME has a clear connection to interstellar dust, but a conclusive link  
15 to any particular population of dust is unapparent.

# 16 **Contents**

17	<b>Abstract</b>	i
18	<b>1 Introduction</b>	2
19	1.1 All-sky Astronomy . . . . .	2
20	1.2 Infrared astronomy . . . . .	2
21	1.3 Microwave foregrounds . . . . .	4
22	1.3.1 Anomalous Microwave Emission . . . . .	5
23	1.3.2 Excitation factors . . . . .	10
24	1.3.3 AME vs. IR in the literature . . . . .	10
25	1.4 Scope of this Dissertation . . . . .	11
26	1.4.1 An application of all-sky archival data . . . . .	11
27	1.4.2 Testing the spinning PAH hypothesis . . . . .	11
28	1.4.3 Limitations . . . . .	11
29	1.4.4 Code availability . . . . .	12
30	<b>2 Data Sources</b>	13
31	2.1 A collection of skies . . . . .	13
32	2.1.1 Primary band of interest . . . . .	13
33	2.2 Infrared Data . . . . .	14
34	2.2.1 AKARI . . . . .	14
35	2.3 Planck COMMANDER Parameter Maps . . . . .	18
36	2.3.1 Synchrotron . . . . .	18
37	2.3.2 Thermal dust emission . . . . .	20
38	2.3.3 COMMANDER-AME: Peak Frequency Distribution . . . . .	20
39	2.4 All-sky Data Processing . . . . .	23

40	<b>3 All-sky Analysis</b>	<b>24</b>
41	3.1 All-sky Pixel Domain Analysis . . . . .	24
42	3.1.1 All-sky cross correlations . . . . .	24
43	3.1.2 Pixel mask . . . . .	24
44	3.1.3 AME data . . . . .	25
45	3.2 Spatial variation of correlations . . . . .	26
46	3.3 Discussion . . . . .	26
47	3.3.1 AME:Dust . . . . .	26
48	3.3.2 AME:PAH . . . . .	29
49	3.3.3 AME: $T, G_0$ . . . . .	30
50	3.3.4 Microwave foreground component separation . . . . .	30
51	<b>4 Analysis of an interesting AME region: <math>\lambda</math> Orionis</b>	<b>31</b>
52	4.1 An interesting AME region . . . . .	31
53	4.1.1 Where does the ring come from? . . . . .	31
54	4.1.2 A well-studied region . . . . .	32
55	4.2 Investigative approach . . . . .	32
56	4.2.1 Data preparation . . . . .	33
57	4.2.2 Extraction from HEALPix maps . . . . .	33
58	4.2.3 Multi-wavelength characterization . . . . .	33
59	4.2.4 Ionization fraction . . . . .	33
60	4.2.5 SED Fitting . . . . .	38
61	4.3 Discussion . . . . .	38
62	4.3.1 AME:PAH . . . . .	38
63	<b>5 Summary</b>	<b>40</b>

# 64 List of Figures

65	1.1	An example of a potential makueup of microwave emission components. Photometry		
66		points are extracted from the Planck and WMAP all-sky maps, for a region well-		
67		known for prominant AME, $\rho$ Ophiuchus. (Planck Collaboration et al. 2011b) . . . . .		5
68	1.2	Two AME prominent regions investigated by Planck Collaboration et al. (2011b);		
69		Tibbs et al. (2011), $\rho$ Ophiuchus and Perseus, as they appear in the AKARI/IRC $9\mu\text{m}$		
70		all-sky data at native resolution. White contours show AME at 1-degree resolution,		
71		extracted from the map by Planck Collaboration et al. (2016b). . . . .		6
72	2.1	AKARI/IRC $9\mu\text{m}$ to IRAS $12\mu\text{m}$ intensity ratio. . . . .		15
73	2.2	AKARI/IRC $9\mu\text{m}$ to IRAS $25\mu\text{m}$ intensity ratio. . . . .		15
74	2.3	Relative spectral response curves of the MIR bands used in this study, AKARI/IRC		
75		$9\mu\text{m}$ , IRAS $12\mu\text{m}$ , WISE $12\mu\text{m}$ , AKARI $18\mu\text{m}$ , and IRAS $25\mu\text{m}$ . AKARI/IRC		
76		$9\mu\text{m}$ , IRAS $12\mu\text{m}$ , WISE $12\mu\text{m}$ bands are dominated by PAH emission. . . . .		16
77	2.4	Ionization fraction of PAHs vs. band ratios of IRAS12 and 25, and WISE 12 and		
78		$25\mu\text{m}$ bads vs. the AKARI $9\mu\text{m}$ band, for three ISRF strengths: Top: $G_0 = 100$ ,		
79		Middle: $G_0 = 1000$ , and Bottom: $G_0 = 10000$ . These ratios are determined by		
80		assuming the SED template if Compiègne et al. (2011) . . . . .		17
81	2.5	$r_s$ cross correlation matrix of the PCCS maps: temperature $T$ , emissivity index $\beta$ , and		
82		amplitude at 545 GHz $I_{dust}(545)$ of thermal dust; intensity of free-free emission $ff$		
83		at ; intensity of synchrotron emisison at 4 MHz $Sync$ ; intensity of the AME var. freq.		
84		component $AME$ at 22.8 GHz. . . . .		19
85	2.6	All-sky map of the ratio of two COMMANDER components- the frequency-varying		
86		AME component divided by the intensity of thermal dust emission at 545 GHz. . . . .		19

87	2.7	The peak frequencies of the varying component $AME_{var}$ . The pink shaded region indicates frequencies not covered by either WMAP or Planck. The green line at 33.5 GHz indicates the peak frequency of $AME_{fix}$ . . . . .	21
90	2.8	All-sky map of the peak frequencies of the varying component $AME_{var}$ , corresponding to Fig. 2.7. . . . .	21
92	2.9	Spdust template spinning dust profiles fitted by PC15X when calculating $AME_{var}$ . The reference frequency, 22.8 GHz is indicated by the vertical green line. Each template has the same $AME_{var}$ amplitude of 100 $\mu\text{K}$ , indicated by the horizontal green line, plotted to highlight the potential deviation between $AME_{var}$ and the actual peak intensity. . . . .	22
97	3.1	Histograms of the peak intensity AME maps calculated from the original COMMANDER-AME reference frequency maps. AMEvar (blue) indicates the distribution of all pixels in the map, with intensities calculated at their peak frequencies (see Fig. . . . .	25
100	3.2	AME intensities vs. peak frequencies. . . . .	26
101	3.3	ALL-SKY cross-correlation matrix for the 12 infrared bands sampled, and the AME map. THe color-scale indicates ( $r_s$ ). Results are based on the full sky (excluding pixels within $10^\circ$ of the ecliptic plane). . . . .	27
104	3.4	ALL-SKY kernel density estimates of 12-band infrared photometry against the PR2 AME map. Pixels within $10^\circ$ of the ecliptic plane are excluded. 'A' indicates AKARI; 'D', DIRBE; 'I', IRAS, and 'P' Planck. The number after each letter indicates the band central nominal wavelength in microns (or frequency in GHz, in the case of the Planck bands.) . . . . .	27
109	3.5	Similar comparison to Fig. 3.4, with both the IR and the AME intensities scaled by the PR2 dust radiance ( $R$ ) for each pixel. . . . .	28
111	3.6	Spatial map of $r_s$ between the AME and IR intensity for 4 bands: 9 $\mu\text{m}$ , 12 $\mu\text{m}$ , 25 $\mu\text{m}$ , and 140 $\mu\text{m}$ . $r_s$ is calculated for all NSIDE 256 pixels within each NSIDE 8 pixel-sized bin. . . . .	28
114	3.7	Spatial map of $r_s$ between the AME and IR intensity as in Fig. 3.6, but with the AME and IR maps first normalized by dust radiance $R$ . . . . .	29

---

116	4.1	$\lambda$ Orionis as it appears in the AKARI 9 $\mu\text{m}$ data. Contours indicate the AME, as given by the Planck PR2 AME map. The image is smoothed to a 1° PSF (much larger than the original 10 arcsec map. The $\lambda$ Orionis star itself is approximately located at the center of the image. . . . .	34
117	4.2	A grid of thumbnails showing the $\lambda$ Orionis region's structure, at 12 wavelengths, along with AME contours (shown in white countours. Spatial correlation seems to be the best at the shortest and longest wavelengths (AKARI/IRC 9 $\mu\text{m}$ and Planck/HFI 550 $\mu\text{m}$ ). The images are smoothed and interpolated for demonstration. Figure 4.1 demonstrates the actual pixel grid used for the SED fitting and intensity correlation tests. . . . .	35
118	4.3	Pixel cross-correlation for all pixels in the $\lambda$ Orionis cut-out region. $r_s$ indicates the Spearman rank correlation coefficient for each plot. . . . .	36
119	4.4	$r_s$ correlation matrix for all of the data used in the $\lambda$ Orionis analysis. . . . .	37
120	1	Explained variance decline for principal component analysis performed on a set of 12 all-sky infrared maps. The first three components account for over 99% of the total variance. The PCA fit is performed on the whole sky, after whitening the data, using the “scikitlearn” . . . . .	43
121			
122			
123			
124			
125			
126			
127			
128			
129			
130			
131			
132			

<sup>133</sup>

# Chapter 1

<sup>134</sup>

## Introduction

<sup>135</sup>

*"It is now plain that about 75% of the data we would like to have can be obtained from good*

<sup>136</sup>

*ground-based sites"*

<sup>137</sup>

-H. Johnson, 1966

<sup>138</sup>

### 1.1 All-sky Astronomy

<sup>139</sup>

All-sky astronomy is not new. Indeed, the notion of capturing a particular “object” or “source” with a camera and saving it for later investigation would be completely alien to the first astronomers and astronavigators. Absence of telescopes forced us to describe the sky in terms of its larger patterns, brightest characters. What is new however is the notion of preparing an archive of the sky itself for not only the research whims of a single investigator, team, institute, or even a single nation rather, all-sky surveys tend to be international endeavors in their production, and even more so in their utilization.

<sup>145</sup>

### 1.2 Infrared astronomy

<sup>146</sup>

Infrared astronomy was essentially non-existent as recently as the 1920s, if we judge by the first IR observations (Pettit & Nicholson 1922, 1928). Mainstream IR astronomy is perhaps much younger, only really taking off - literally- in the post-war era, via balloon and rocket borne experiments (Johnson 1966). Compare this to visible wavelengths, a field so old we name it after the bio-evolutionary advent of sight, itself. Even radio astronomy with its own logistical and technological challenges, has been around since at least 1932.

<sup>152</sup>

Despite the title quote above, astronomers were apparently not content to be constrained by atmo-

153 spheric IR windows, even from the best of ground-based sites. Or perhaps interests have shifted so  
 154 dramatically since 1966, that all of the investigations enabled by rocket-based, space-based, even Boe-  
 155 ing 747-based IR astronomy (Young et al. 2012) would have bored 75% of astronomers in the '60s.  
 156 The meaning of "far infrared" has even redshifted, so to speak, from the Johnson (1966) definition of  
 157 "4 to 22  $\mu\text{m}$ ".

158 For our purposes, we consider the FIR to cover 60 to 550  $\mu\text{m}$ , partially out of convenience- FIR  
 159 bands, in this paper, means the IRAS 60 and 100 micron, all four FIS bands, and the HFI 857 GHz and  
 160 545 GHz bands. The two IRC bands and the IRAS 12 and 25  $\mu\text{m}$  bands we will refer to collectively  
 161 as the MIR bands.

162 The ability to map and archive the sky with satellites - not only in the optical and infrared, but  
 163 well into the microwave regime - has enabled interdisciplinary research of the ISM. The merits of  
 164 multiwavelength based investigations arise from the simple fact that the ISM is very complex- both in  
 165 terms of the myriad forms of matter present - from plasmas to dust grains - and in countless physical  
 166 processes at play.

167 Consider the case of a dusty plasma, as in a supernova remnant or Hii region around an

168 Studies of optical transients - a field accessible to amateur astronomers - can be validated by  
 169 follow-ups in the infraredMulti-wavelength investigations not only allow us to examine the particular  
 170 source we are interested in, but let us paint a full astrophysical picture. This is because the studying  
 171 a given astrophysical phenomenon quickly requires us to control for confusing factors. Consider the  
 172 case of thermal dust emission: attempting to trace the peak of thermal equilibrium dust emission, we  
 173 will soon encounter deviations on the Wiens side- we know now that these mid to near IR deviations  
 174 likely come from a smaller population of interstellar dust grains, with lower heat capacities (Purcell  
 175 1976; Sellgren 1984; Dwek 1986; Draine & Li 2001).

176 Astrochemists study of the molecular landscape of the ISM are

177 Astrophysicists focused on the Milky Way itself are collaborating closely with those having more  
 178 distant goals. Johnson (1966) did not offer a definition of "microwave", though Penzias & Wilson  
 179 (1965) had stumbled into microwave astronomy a year before in their chance discovery of the cosmic  
 180 microwave background (CMB). The CMB itself being relatively easy to model, on its own - latest  
 181 measurements by Had the CMB been the only astronomical source of emission however, there would  
 182 be no need for the following sections.

---

 183 **1.3 Microwave foregrounds**

184 The study of our galaxy itself via microwave emission is surely worth chapters of discussion. The  
 185 reason that galactic microwave emission has gotten the amount of attention it has in recent years  
 186 however has little to do with galactic astronomy. Rather, our galaxy presents an inconvenience to  
 187 observational cosmology in that it 'contaminates' observations of the CMB. The average SED of  
 188 the CMB is simple enough to model, with a 2.755 K blackbody function. This temperature however  
 189 means that the peak occurs between several microwave foreground components, as displayed in Fig.  
 190 1.1.

191 temperature puts its emission peak right in the middle of severalThe difficult of decomposing  
 192 the microwave sky into galactic ISM, extragalactic, and CMB components has brought the detailed  
 193 decomposition of the microwaveradio regime of ISM to the forefront of Planck Collaboration paper  
 194 titles (Planck Collaboration et al. 2011a, 2014a, 2016a). This is true even though the CMB itself is  
 195 relatively simple to model theoretically. - in the combined papers of the official numbered Planck Col-  
 196 laboration paper series, the word "dust" appears in 20; "Galactic" in 23; "Galactic dust" in 5. Without  
 197 extragalactic research, there would be no need for the word "foreground" in describing galactic mi-  
 198 crowave emission.

199 The ISM has intruded into cosmological studies perhaps most prominently with the first claimed  
 200 detection of B-mode polarization (Hanson et al. 2013; BICEP2 Collaboration et al. 2014; Flauger et al.  
 201 2014) and the subsequent counterclaim that this detection arose from galactic dust, and most recently  
 202 the counter-counter suggestion that, after carefully accounting for galactic dust, the combined BI-  
 203 CEP2/Planck detection of B-mode polarization appears validated (Planck Collaboration et al. 2017).<sup>1</sup>.  
 204 Similarly, More recently AMI Consortium et al. (2012) had noted a peculiar SunyaevZeldovich effect  
 205 based galaxy cluster detection, AMI-CL J0300+2613. Perrott et al. (2018) have since proposed that  
 206 this may in fact arise from high galactic latitude dust via "anomalous microwave emission" (AME  
 207 is described in the next section). In this way, enhanced wavelength coverage is both enabling and  
 208 requiring deeper cross-disciplinary (galactic, extragalactic, CMB) collaboration.

---

<sup>1</sup>see Sheehy & Slosar (2017) for another take on Planck B-mode detection significance

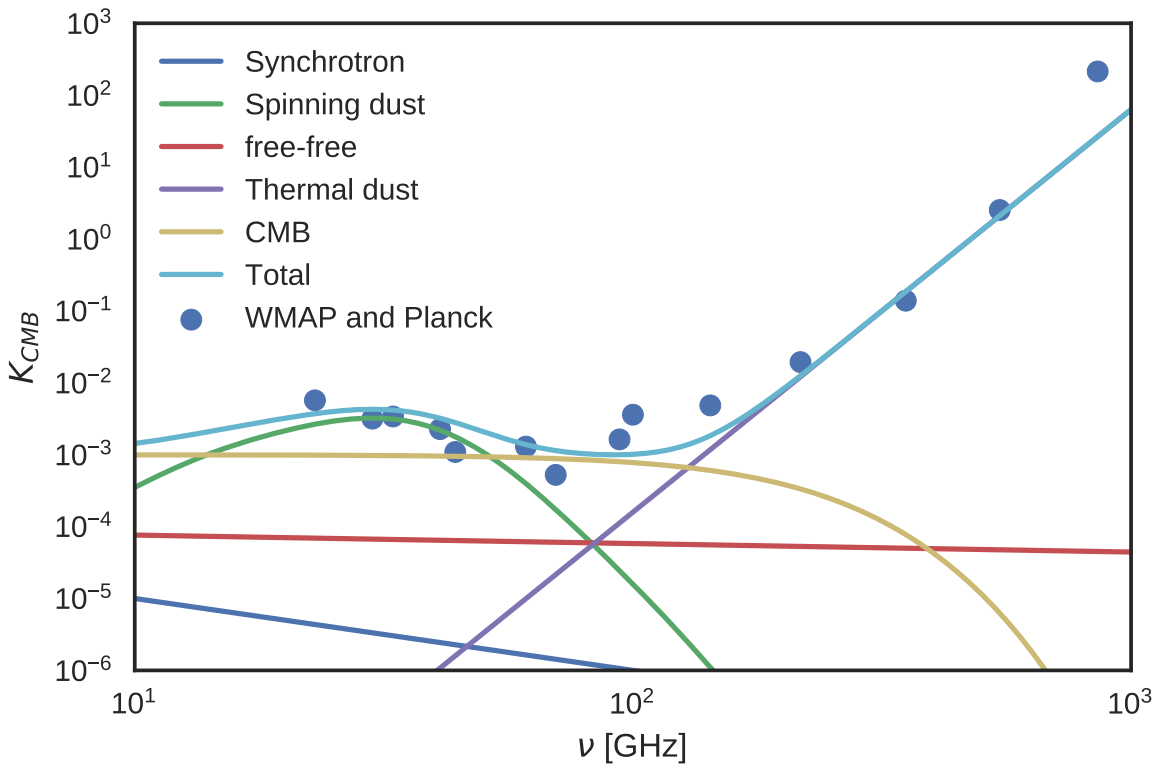


Figure 1.1: An example of a potential makueup of microwave emission components. Photometry points are extracted from the Planck and WMAP all-sky maps, for a region well-known for prominent AME,  $\rho$  Ophiuchus. (Planck Collaboration et al. 2011b)

### 209 1.3.1 Anomalous Microwave Emission

210 In our efforts to decompose and understand galactic microwave emission itself, there remains a con-  
 211 stant antagonist. Anomalous microwave emission (AME) is a component of microwave emission in  
 212 excess of 10 to 40 GHz predictions for known microwave emission mechanisms, lacking a confirmed  
 213 physical mechanism. The term itself can be a bit confusing, as the word “anomalous” tends to im-  
 214 ply an outlier lacking much evidence as to its cause, and with few empirical patterns. In this section  
 215 we will explain that while there is indeed much mystery as to the exact mechanism(s) producing the  
 216 AME, what causes its spectral variations, and what might be its physical carrier(s) - it is by now, per-  
 217 haps less than anomalous. Following subsections will discuss the history of AME and the produced  
 218 physical explanations, as well comparisons between the AME and infrared emission from interstellar  
 219 dust.

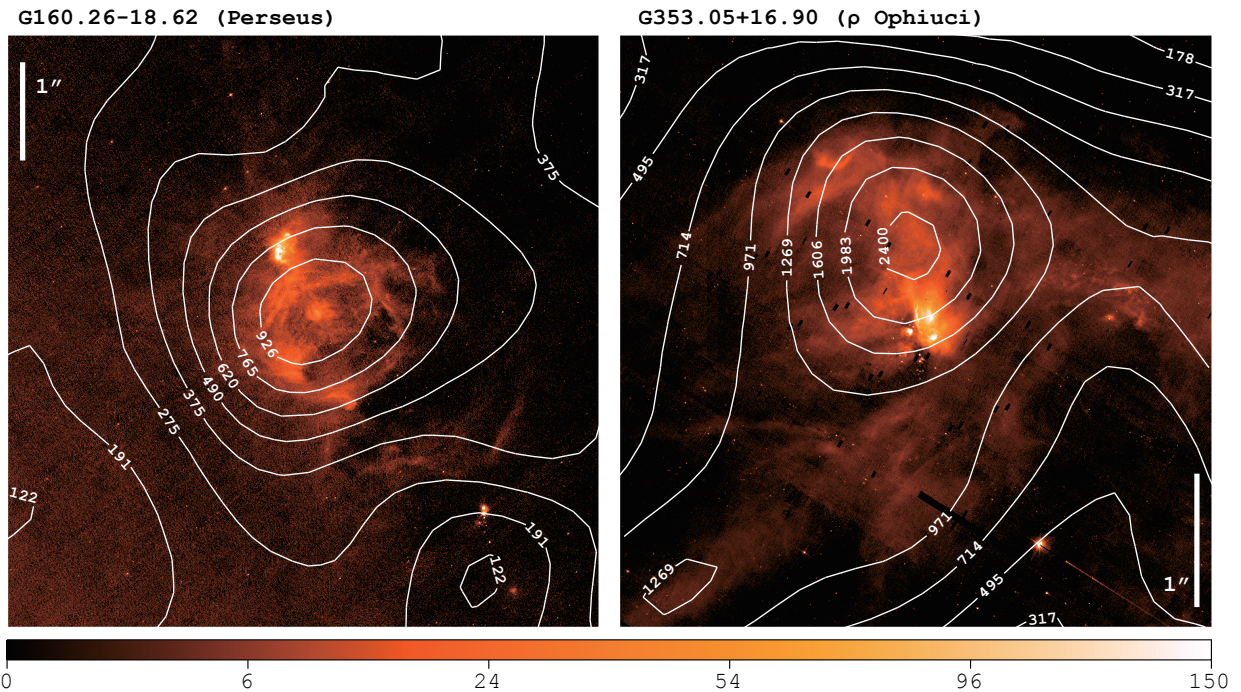


Figure 1.2: Two AME prominent regions investigated by Planck Collaboration et al. (2011b); Tibbs et al. (2011),  $\rho$  Ophiuchus and Perseus, as they appear in the AKARI/IRC  $9\mu\text{m}$  all-sky data at native resolution. White contours show AME at 1-degree resolution, extracted from the map by Planck Collaboration et al. (2016b).

---

**220 Discovery and first explorations**

221 Since its first detection in early microwave observations, AME has been found to be a widespread  
 222 feature of the microwave Milky Way (Dickinson et al. 2013). Kogut et al. (1996); de Oliveira-Costa  
 223 et al. (1997); Leitch (1998) showed that the AME correlates very well with infrared emission from  
 224 dust, via COBE/DIRBE and IRAS far-IR maps.

225 From about 2002, the AME starts to become less of an anomaly, and more of an established -albeit  
 226 mysterious- component of microwave emission. Finkbeiner et al. (2002) reported the first detection  
 227 of a “rising spectrum source at 8–10 GHz” in a targeted observation, making the AME more than  
 228 a statistical spectral outlier in CMB experiments. de Oliveira-Costa et al. (2002) further argued that  
 229 this emission is in fact “ubiquitous”. The exact mechanism and carrier/s remain mysterious however.

230 Variations in the spectral profile of the AME signature,

231 However there remains much mystery, except that the most likely source of the AME is interstellar  
 232 dust. Several works have reported correlations between AME and thermal dust emission - but with  
 233 some disagreement as to whether this correlation is improved in  $12\ \mu\text{m}$  emission vs.  $100\ \mu\text{m}$  emission  
 234 (Ysard & Verstraete 2010; Tibbs et al. 2011; Hensley et al. 2016). Exactly which physical mecha-  
 235 nisms are at play is still an open question, even if we assume a dusty AME origin. Even assuming a  
 236 particular dust-based physical mechanism, we would still be puzzled as to the chemical composition  
 237 and morphology of the carrier(s). We also lack an all-sky constraint on the emissivity of the AME  
 238 spectrum at frequencies short of the WMAP cut-off, around 23 GHz.

239 **Proposed explanations**

240 From the observed spatial correlation between AME and dust emerged two prevailing hypotheses:  
 241   1) Electric dipole emission by spinning small dust grains, a mechanism proposed in Erickson  
 242 (1957) and Hoyle & Wickramasinghe (1970), with further discussion in Ferrara & Dettmar (1994).  
 243 Draine & Lazarian (1998b) give the earliest thorough description, with substantial updates contributed  
 244 more recently by Ysard & Verstraete (2010), Ali-Haïmoud et al. (2009), Hoang et al. (2010) and  
 245 several others. Hensley & Draine (2017a) propose that such small spinning grains may consist pri-  
 246 marily of silicates, and that this is allowed by observational upper-bounds of nanosilicate abundance,  
 247 although nanosilicates have not yet been detected in the ISM. Dickinson et al. (2013) provide a de-  
 248 tailed overview of AME and spinning dust literature. An updated state of play of AME research has  
 249 been submitted at the time of this writing (Dickinson, et al., submitted). Eq. 1.3.1 gives the radiated

250 power by spinning dust

$$P = \frac{4}{9} \frac{\mu^2 \omega^4}{c^3} \quad (1.3.1)$$

$$\frac{\omega_T}{2\pi} = \langle \nu^2 \rangle^{1/2} \approx 5.60 \times 10^9 a_{-7}^{-5/2} \xi^{-1/2} T_2^{1/2} \text{ Hz} \quad (1.3.2)$$

251 2) Magnetic dipole emission, caused by thermal fluctuations in grains with magnetic inclusions,  
 252 proposed by Draine & Lazarian (1999). More recently, modeled spectra for potential candidate carri-  
 253 ers have appeared in the literature: PAHs, grains with magnetic inclusions (Draine & Hensley 2013;  
 254 Ali-Haïmoud 2014; Hoang et al. 2016).

255 A third, but not widely accepted, possible explanation for AME is discussed in Jones (2009).  
 256 They have suggested that the emissivity of dust, in the spectral range related to AME, could contain  
 257 features caused by low temperature solid-state structural transitions.

## 258 Spinning dust

259 Spinning dust need not be the only emission mechanism, a convention as arisen in AME observational  
 260 works. The photometric signature of the AME is frequently interpreted via spinning dust parameters  
 261 (Ysard et al. 2011; Ali-Haimoud 2010). Archival all-sky AME data products exclusively assume a  
 262 spinning dust SED templates.<sup>2</sup> Using the “spdust” spinning dust SED model code to fit excess  
 263 microwave foreground emission has become as commonplace as fitting a modified blackbody function  
 264 to the far IR.

265 We explore the case that the AME signature arises from spinning dust emission. If the AME  
 266 is carried by spinning dust, the carrier should be small enough that it can be rotationally excited to  
 267 frequencies in the range of 10-40 GHz, and must have a permanent electric dipole. Within contem-  
 268 porary dust SED models, only the polycyclic aromatic hydrocarbon family of molecules (PAHs), or  
 269 nanoscale amorphous carbon dust fit these criteria. Those PAHs which have a permanent electric  
 270 dipole (i.e. coronulene, but not symmetric molecules like coronene), can emit rotationally. However  
 271 the carrier need not be carbon-based. Indeed, Hensley & Draine (2017a) claim that AME can be  
 272 explained without carbonaceous carriers, using only spinning nanosilicates.

---

<sup>2</sup>Both WMAP and Planck used a base template with 30 GHz peak frequency, and an assumed cold neutral medium environment.

---

273 Spinning PAHs?

274 Assuming the rotational emission model of Draine & Lazarian (1998b), the AME signature (consis-  
 275 tent with peaked, continuum emission having a peak between 15 and 50 GHz ) implies very small  
 276 oscillators ( $\sim 10$  nm).

277 In any case, the PAH class of molecules are the only spinning dust candidate so far which show  
 278 both:

279 1) Evidence of abundance in the ISM at IR wavelengths, and  
 280 2) A predicted range of dipole moments (on order of 1 debye), to produce the observed AME signature  
 281 (Draine & Lazarian 1998b; Lovas et al. 2005; Thorwirth et al. 2007). However, it should be noted  
 282 that the current upper-bound on the abundance of nanosilicates, allows for a "spinning nanosilicate"  
 283 explanation for the AME, as shown by Hensley & Draine (2017a). Due to the (apparently) continuous  
 284 shape of the AME SED, a spinning dust explanation requires a distribution of dipole moments and/or  
 285 rotational velocities of the carriers. Of course, the AME cannot simply be modeled by a distribution of  
 286 carriers. Environmental factors affecting the rotational excitation of the carriers must be considered.

287 **A more testable hypothesis** At the time of this writing, there is no strong argument in the literature  
 288 that either PAHs or nanosilicates are physically preferred by AME observations. The physical plausi-  
 289 bility of rapidly spinning PAHs and of rapidly spinning nanosilicates to produce the AME have both  
 290 been outlined. This plausibility however is contingent on the abundance of PAHs or nanosilicates  
 291 with appropriate dipole moments, and in regions with suitable excitation environments.

292 The arguments for or against particular carriers of the AME come from carrier abundance es-  
 293 timates and their statistical comparison with AME estimates. While neither nanosilicates nor any  
 294 particular species of PAHs have been conclusively identified in the ISM, there is far more empirical  
 295 evidence for PAH-like dust than for nanosilicates. Mid-infrared features associated with PAH-like  
 296 aromatic materials have been observed. In fact, "the PAH features" are ubiquitous in the ISM (Giard  
 297 et al. 1994; Onaka et al. 1996; Onaka 2000), such that the carriers must be abundant.<sup>3</sup> There has yet  
 298 to be any detection of features related to nanosilicates. There is only an upper-bound from IRTS ob-  
 299 servations of Onaka et al. (1996) and calculations by Li & Draine (2001). Hensley & Draine (2017a)  
 300 argue that this upper-bound does not prohibit nanosilicates as the sole carriers of the AME.

---

<sup>3</sup>Andrews et al. (2015) strongly argue for the existence of a dominant "grandPAH" class, containing 20 to 30 PAH species.

---

### 301 1.3.2 Excitation factors

302 In the spinning dust model, there are several possible excitation factors for spinning dust. For the  
 303 grains to have rotational velocities high enough to create the observed AME, they must be subject  
 304 to strong excitation mechanisms. The dominant factors that would be giving grains their spin, are  
 305 broken down by Draine (2011) into basically two categories: 1) Collisional excitation. 2) Radiative  
 306 excitation, the sum of which could lead to sufficient rotational velocities for sufficiently small grains.  
 307 However the extent of excitation will depend on environmental conditions, i.e. there will be more  
 308 frequent encounters with ions and atoms in denser regions (so long as the density is not high enough  
 309 to coagulate the small grains), and more excitation due to photon emission with increasing ISRF  
 310 strength (Ali-Haïmoud et al. 2009; Ali-Haïmoud 2014). One of the strongest potential excitation  
 311 mechanisms listed in Draine (2011) is that of negatively charged grains interacting with ions. Thus  
 312 not only must we consider environmental factors, grain composition and size, but also the ionization  
 313 state of the carriers. (For example, ionized vs. neutral PAHs.) The dependence of the observed AME  
 314 on ISM density is modeled by Ali-Haimoud (2010), demonstrating that denser regions may have a  
 315 stronger AME component (although it can be observationally challenging to resolve dense vs. diffuse  
 316 AME producing regions.)

### 317 1.3.3 AME vs. IR in the literature

318 The overall pattern among large-scale studies seems to show that all of the dust-tracing photometric  
 319 bands correlate with the AME (and each other) to first-order. On an all-sky, pixel-by-pixel basis,  
 320 at  $1^\circ$  angular resolution, Ysard et al. (2010) find that  $12\ \mu\text{m}$  emission, via IRAS, correlates slightly  
 321 more strongly with AME (via WMAP) than with  $100\ \mu\text{m}$  emission. They also find that scaling the  
 322 IR intensity by the interstellar radiation field strength (given as  $G_0$ , a measure of ISRF relative to that  
 323 of the solar neighborhood) improves both correlations. They interpret this finding as evidence that  
 324 AME is related to dust, and more closely related to the small stochastically emitting dust that is traced  
 325 by  $12\ \mu\text{m}$  emission.

326 However in a similar work, Hensley et al. (2016) report that the  $12\ \mu\text{m}$  emission (via WISE)  
 327 correlates less tightly with AME than with thermal dust radiance, using the Planck Collaboration  
 328 dust and AME component-separation maps (Planck Collaboration et al. 2016b). Also at odds with  
 329 Ysard et al. (2010), they report that AME correlates more strongly with  $12\ \mu\text{m}$  intensity than with the  
 330 intensity scaled by the interstellar radiation field. They interpret this as AME and PAH emission both

331 being correlated with the total dust radiance, but that there is no preferential relationship between  
 332 PAHs and the AME.

333 The story is no more clear when looking at the average properties of individual regions. Planck  
 334 Collaboration et al. (2014d) find that among 22 high-confidence "AME regions" (galactic clouds  
 335 such as the  $\rho$  Ophiuchus cloud and the Perseus molecular cloud complex) AME vs.  $12 \mu\text{m}$  shows a  
 336 marginally weaker correlation than AME vs.  $100 \mu\text{m}$  (via IRAS). Tibbs et al. (2011) examined the  
 337 AME-prominent Perseus Molecular Cloud complex, finding that while there is no clear evidence of a  
 338 PAH-AME correlation, they do find a slight correlation between AME and  $G_0$ .

## 339 1.4 Scope of this Dissertation

### 340 1.4.1 An application of all-sky archival data

341 This is an astrophysical data archive based work. The primary goal is to highlight a particular ap-  
 342 plication of multiwavelength (mid-IR to radio), cross-archive all-sky data analysis. We describe the  
 343 interrelatedness between mid to far IR dust emission and possible microwave emission from dust.  
 344 This is accomplished through an investigation of photometric all sky maps mainly from AKARI,  
 345 IRAS, and Planck.

### 346 1.4.2 Testing the spinning PAH hypothesis

347 For the present work, we consider the spinning PAH hypothesis to have the highest degree of testabil-  
 348 ity, due to the well-established presence of aromatic emisison feaetures in the ISM. We do not argue  
 349 against the physical plausibility of nanosilicates to produce the AME. Indeed, there is no argument to  
 350 date that these potential physicalities are mutally exclusive, as long as both potential carriers are suf-  
 351 ficiently abundant. Nor does spinning dust emission theoretically exclude magnetic dipole emission  
 352 or microwave thermal dust emissivity fluctuations.

### 353 1.4.3 Limitations

354 We do not explore the modeling of microwave dust emission itself, rather the comparison of existing  
 355 archival data and parameter maps. Modeling of the exact physical mechanism of the anomalous  
 356 component of galactic microwave foreground emission from first principles is beyond the scope of

357 this work. We consider this problem first on an all-sky basis, not focusing on any pre-selected object  
358 of the sky - in order to assess if there any general pattern between the IR and the AME, beyond  
359 the AME-dust correlation already described above. We then focus on a region highlighted by the  
360 Planck Collaboration as being especially worthy of further investigation (Planck Collaboration et al.  
361 2016b), and has a resolvable topology even at 1-degree resolution. Essentially all of the analyses and  
362 conclusions presented in this work apply to an angular scale of approximately 1-degree, and only for  
363 the given component separation methods (Solar system, galactic, extragalactic) used by each of the  
364 data providers.

#### 365 1.4.4 Code availability

366 This dissertation is accompanied by a github repository<sup>4</sup> Virtually all of the analyses code are available  
367 in that repository, in the form of Jupyter notebooks (along with the figures and the code used to  
368 generate them.) The dust SED fitting code is not part of that repository, but is described in Galliano  
369 et al. (in prep.)

---

<sup>4</sup>Available at: <https://github.com/aaroncnb/CosmicDust>.

# <sup>370</sup> Chapter 2

## <sup>371</sup> Data Sources

### <sup>372</sup> 2.1 A collection of skies

<sup>373</sup> This work relies completely on all-sky surveys. All of the maps utilized are photometric-band infrared  
<sup>374</sup> maps, except for the AME data, which is an all-sky component separation analysis product, from the  
<sup>375</sup> Planck Collaboration’s efforts to separate galactic foregrounds from the CMB.

Table 2.1: Observational data sources used in this article

Instrument	Central Wavelength	FWHM	Cali	Reference
AKARI/IRC	9 $\mu\text{m}$	$\sim 10''$	<10%	<sup>1</sup>
AKARI/IRC	18 $\mu\text{m}$	$\sim 10''$	<10%	"
AKARI/FIS	65 $\mu\text{m}$	63''	<10%	<sup>2</sup>
AKARI/FIS	90 $\mu\text{m}$	78''	<10%	"
AKARI/FIS	140 $\mu\text{m}$	88''	<10%	"
AKARI/FIS	160 $\mu\text{m}$	88''	<10%	"
IRAS/IRIS	12 $\mu\text{m}$	4.0'	<5.1%	<sup>3</sup>
IRAS/IRIS	25 $\mu\text{m}$	4.0'	<15.1%	"
IRAS/IRIS	60 $\mu\text{m}$	4.2'	<10.4%	"
IRAS/IRIS	100 $\mu\text{m}$	4.5'	<13.5%	"
Planck/HFI	345 $\mu\text{m}$	4.7'		<sup>4</sup>
Planck/HFI	550 $\mu\text{m}$	4.3'		"

#### <sup>376</sup> 2.1.1 Primary band of interest

<sup>377</sup> <sup>5</sup> The AKARI/IRC 9  $\mu\text{m}$  band (A9) provides uniquely complete coverage of the PAH bands at 6.2,  
<sup>378</sup> 7.7, 8.6, and 11.2  $\mu\text{m}$ , and may be an excellent tool for testing PAH-related hypotheses on an all-sky

<sup>1</sup>(Ishihara et al. 2010)

<sup>2</sup>Doi et al. (2015); Takita et al. (2015)

<sup>3</sup>Miville-Deschénes & Lagache (2005)

<sup>4</sup>Planck Collaboration et al. (2014b)

<sup>5</sup>Not to be confused with “The band primarily interested” in dust, Queen.

379 basis. The combination of A9 with W12 and/or I12 may be especially insightful. In total, we employ  
 380 all-sky maps from 12 photometric bands, spanning the wavelength range of  $6.9 \mu\text{m}$  to  $550 \mu\text{m}$ <sup>6</sup>

## 381 2.2 Infrared Data

### 382 2.2.1 AKARI

383 The AKARI infrared space telescope revealed an entire sky of infrared light, from the mid to far  
 384 infrared, via two instruments (Murakami et al. 2007) the Infrared Camera (IRC)(Onaka et al. 2007)  
 385 and the Far Infrared Surveyor (FIS) (Kawada et al. 2007a).

386 **AKARI/IRC PAH feature coverage** The IRC's  $9 \mu\text{m}$  band all-sky map demonstrates the abun-  
 387 dance of the PAH bands carrier in the Milky Way (Ishihara et al. 2010). Figure 2.3 shows the coverage  
 388 of the MIR bands along with an example galactic cirrus SED. The  $9 \mu\text{m}$  band uniquely covers major  
 389 ionized PAH features at  $6.2$  and  $7.7 \mu\text{m}$ ; as well as neutral PAH features at  $8.6$  and  $11.2 \mu\text{m}$  across  
 390 the entire sky (Onaka et al. 2007). The IRAS  $12 \mu\text{m}$  band covers the  $11.2$  and  $8.6 \mu\text{m}$  features, and  
 391 the similarly-shaped WISE  $12 \mu\text{m}$  band covers primarily the  $11.2 \mu\text{m}$  feature.

392 **In-band contribution from PAHs** According to this distribution of PAH features across the re-  
 393 sponse filters, it is expected that the IRC  $9 \mu\text{m}$  band is most dominated by PAH emission even with  
 394 increasing  $G_0$ . These contributions remain relatively constant out to a  $G_0$  of about 100, with the con-  
 395 tribution from warm dust becoming a larger factor for the IRAS  $12 \mu\text{m}$  and WISE  $12 \mu\text{m}$  bands.  
 396 Thus, according to the DL01 template, IRC  $9 \mu\text{m}$  should have the highest contribution from PAHs  
 397 out to extreme radiation fields.

398 **Potential to trace PAH ionization** Fig. 2.4 demonstrates how the band ratios of the IRC 9um band  
 399 vs. the other MIR bands change with different modeled PAH ionization fractions (determined using  
 400 the DustEM default model template, by Compiègne et al. (2011)). This band ratio can be determined,  
 401 because the IRC9 filter is more sensitive to ionized PAH features, relative to IRAS12 or to WISE12.  
 402 IRC  $9 \mu\text{m}$  shows a larger contribution from ionized PAHs, by about 16 percent, and a conversely  
 403 smaller contribution from neutral PAHs. Figs. 2.1 and 2.2 show the R(A9:I12) and R(A9:I25) ratio  
 404 maps.

---

<sup>6</sup>Planck bands are named according to their central frequency, not wavelength.

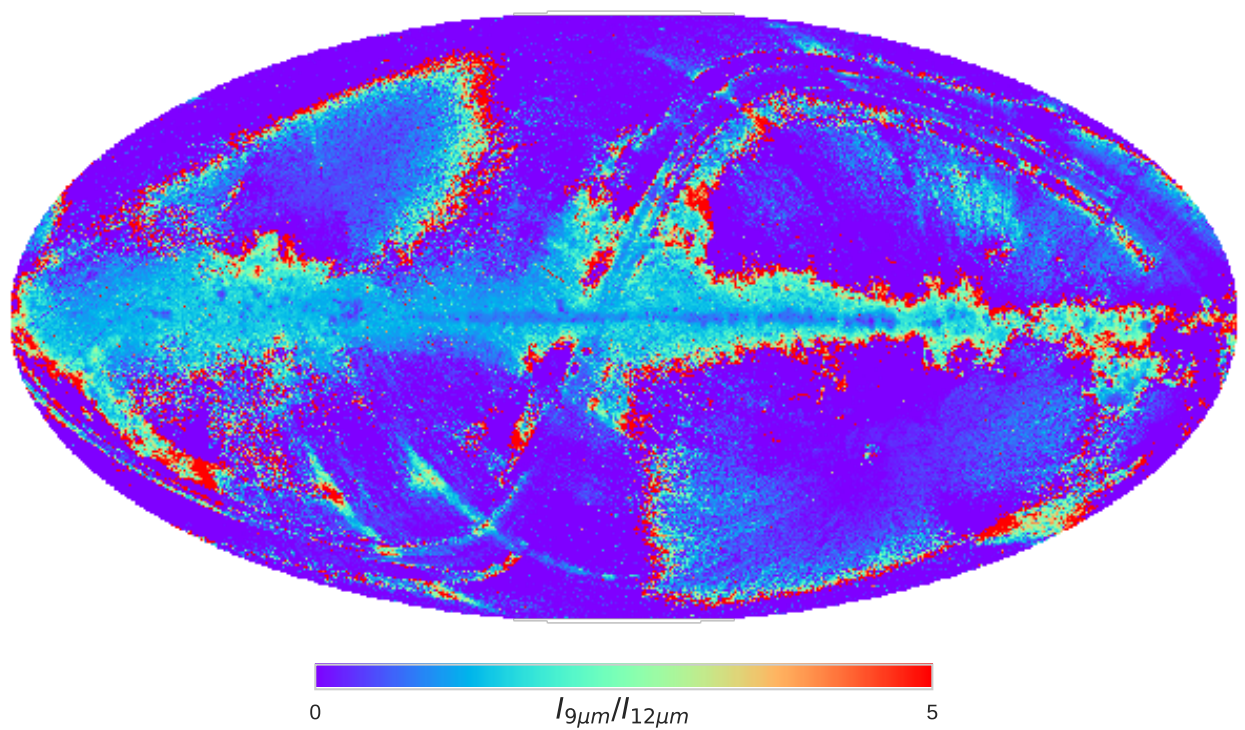


Figure 2.1: AKARI/IRC 9  $\mu\text{m}$  to IRAS 12  $\mu\text{m}$  intensity ratio.

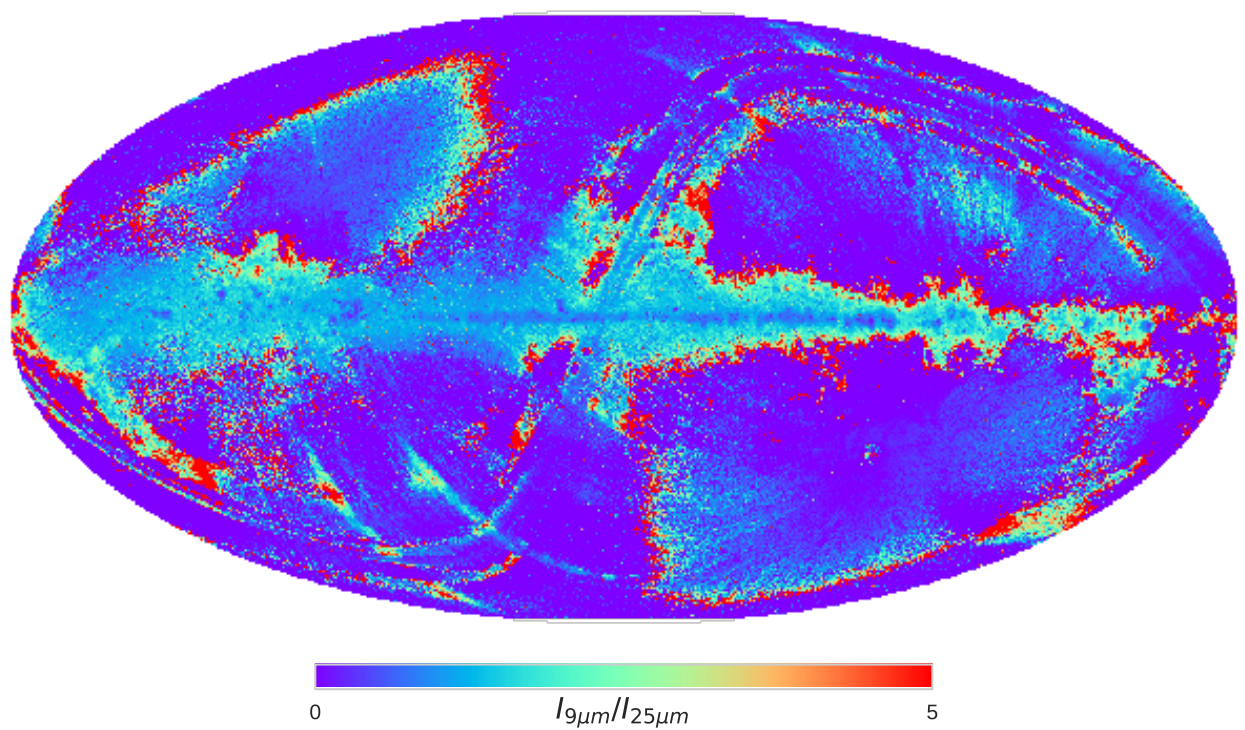


Figure 2.2: AKARI/IRC 9  $\mu\text{m}$  to IRAS 25  $\mu\text{m}$  intensity ratio.

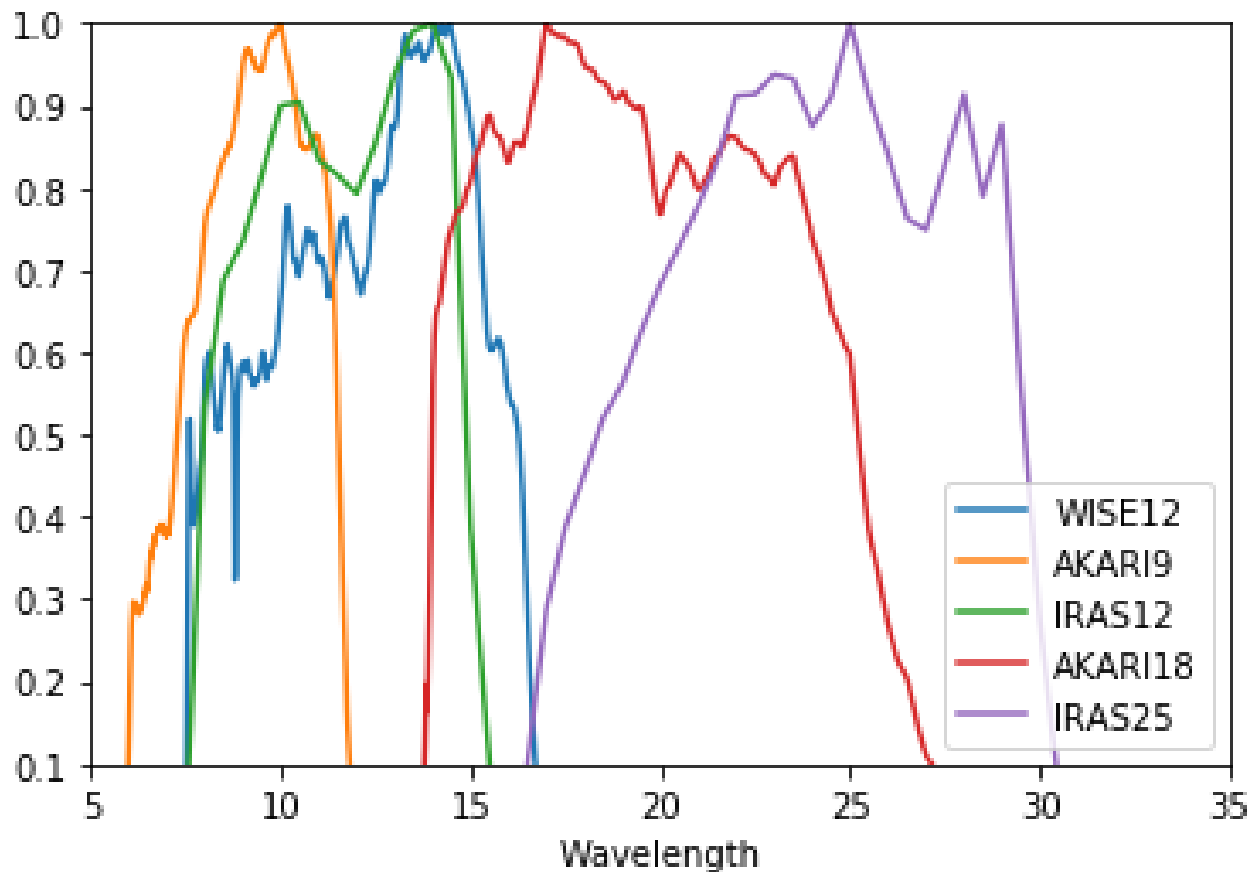


Figure 2.3: Relative spectral response curves of the MIR bands used in this study, AKARI/IRC 9  $\mu\text{m}$ , IRAS 12  $\mu\text{m}$ , WISE 12  $\mu\text{m}$ , AKARI 18  $\mu\text{m}$ , and IRAS 25  $\mu\text{m}$ . AKARI/IRC 9  $\mu\text{m}$ , IRAS 12  $\mu\text{m}$ , WISE 12  $\mu\text{m}$  bands are dominated by PAH emission.

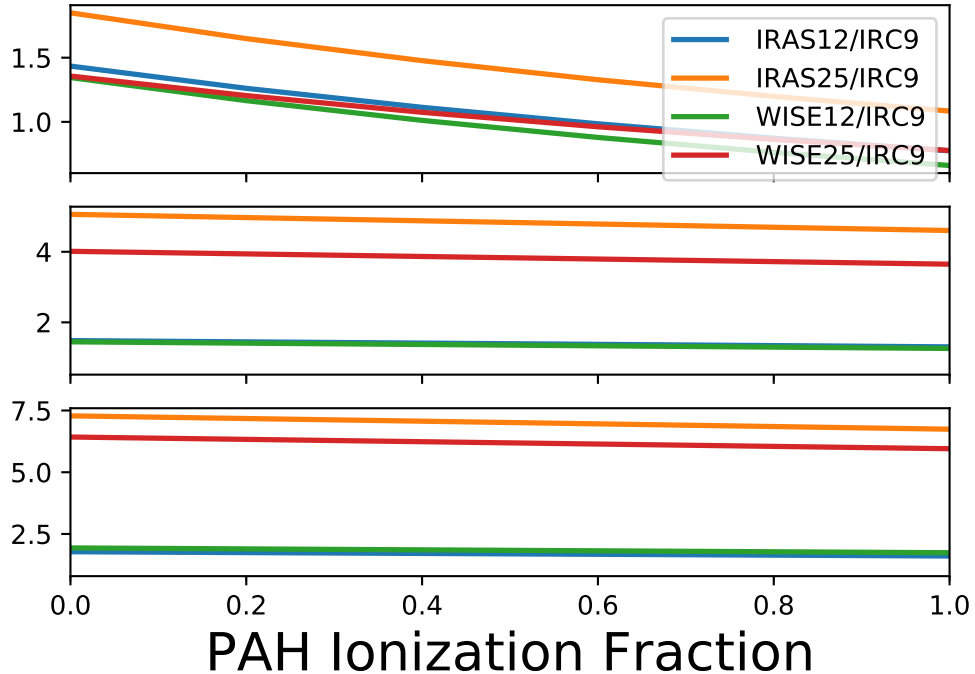


Figure 2.4: Ionization fraction of PAHs vs. band ratios of IRAS12 and 25, and WISE 12 and 25  $\mu\text{m}$  bands vs. the AKARI 9  $\mu\text{m}$  band, for three ISRF strengths: Top:  $G_0 = 100$ , Middle:  $G_0 = 1000$ , and Bottom:  $G_0 = 10000$ . These ratios are determined by assuming the SED template of Compiègne et al. (2011)

405 We utilize the most recent version of the IRC data (Ishihara, et al., in prep.) This version has  
 406 had an updated model of the Zodiacial light, fitted and subtracted. The details of the improved Zodi-  
 407 model, which offers an improvement over that used for the IRAS all-sky maps, are given in Kondo  
 408 et al. (2016).

409 The AKARI Far Infrared Surveyor (FIS) gives us photometric data around the peak of the typical  
 410 thermal dust SED. FIS was equipped with four wavebands: two narrow bands centered at 65  $\mu\text{m}$  and  
 411 at 160  $\mu\text{m}$ , and two wide bands at 90  $\mu\text{m}$  and at 140  $\mu\text{m}$ . An all-sky survey was carried out at each  
 412 band (Kawada et al. 2007b), and the processed maps have been publicly released (Doi et al. 2015).

413 The Planck Space Observatory (Planck) High Frequency Instrument (HFI) all-sky maps, spanning  
 414 100 to 857 GHz (Planck Collaboration et al. 2014b) help constrain the far IR dust emissivity. This  
 415 study utilizes the 857 GHz (345  $\mu\text{m}$ ) and 545 GHz (550  $\mu\text{m}$ ) bands.

416 Data from the Infrared Astronomical Satellite (Neugebauer et al. 1984) all-sky surveys are used  
 417 to supplement the similarly-centered AKARI photometric bands. The IRAS 12  $\mu\text{m}$  band is similar to  
 418 the AKARI 9  $\mu\text{m}$  band in terms of the sky coverage, central wavelength, and especially in that both  
 419 surveys are heavily dominated by zodiacal light. We use the Improved Reprocessing of the IRAS  
 420 Surveys (IRIS) (Miville-Deschénes & Lagache 2005), which use undergone a zodiacal-light removal.

421 The Zodiacal light model, however differs between the two bands. The IRAS Zodi-subtraction is  
422 primarily based on the Kelsall et al. (1998) model.

## 423 2.3 Planck COMMANDER Parameter Maps

424 We utilize the COMMANDER-Ruler astrophysical component separation maps, from the Planck  
425 Collaboration's Public Data Release 2 (hereafter, PR2). These contain estimates of known microwave  
426 foreground components (free-free, synchrotron, thermal dust emission contributions to the Planck  
427 photometric bands. Details of the foreground contribution estimates are given in Planck Collaboration  
428 et al. (2014c). Fig. 2.5 demonstrates the correlatedness of these component maps, taken as provided  
429 in the PR2 archive. Without considering noise levels or variations of scale, we see evidence these  
430 major components are correlated with one another. In the case of free-free emission, von Hausegger  
431 & Liu (2015) found that by taking S/N ratios into account, the correlation between COMMANDER  
432 free-free and AME components turns negative. More generally they suggest that the intercorrelations  
433 between these products varies with scale. We will first describe the 'non-AME' components, so as to  
434 not give any indication that their estimation is trivial.

### 435 2.3.1 Synchrotron

436 While the Planck observations themselves do limit our resolution when assessing the AME - it is in  
437 fact the primary constraint on synchrotron emission, 408 MHz map by Haslam et al. (1982) that is  
438 the major resolution limiting factor. While an impressive, pioneering effort to reveal the low-  
439 frequency sky, (Haslam et al. 1982) is limited to an approximately 1 degree resolution. The map also  
440 contains many artifacts. For the time being however, it is still the most synchrotron-dominated all-sky  
441 map available, and for this reason PC15X included it in their COMMANDER component separation.  
442 The final synchrotron product produced by COMMANDER (hereafter, PCSync) highly resembles  
443 the (Haslam et al. 1982) map, however it is also demonstrated PCSync does not fully capture the  
444 synchrotron signal. This can be visualized by inspecting the PCAME:PCdust ratio map (see Fig. 2.6),  
445 which Hensley et al. (2016) describe as containing synchrotron emission patterns at high latitudes.

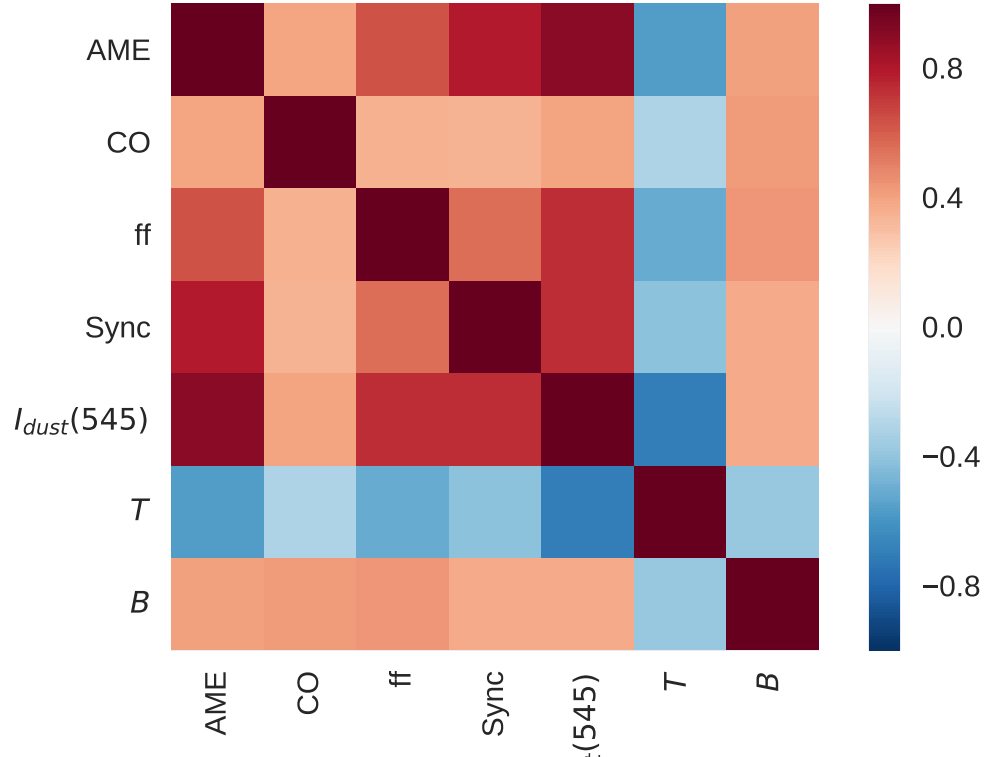


Figure 2.5:  $r_s$  cross correlation matrix of the PCCS maps: temperature  $T$ , emissivity index  $\beta$ , and amplitude at 545 GHz  $I_{dust}(545)$  of thermal dust; intensity of free-free emission  $ff$ ; intensity of synchrotron emission at 4 MHz  $Sync$ ; intensity of the AME var. freq. component  $AME$  at 22.8 GHz.

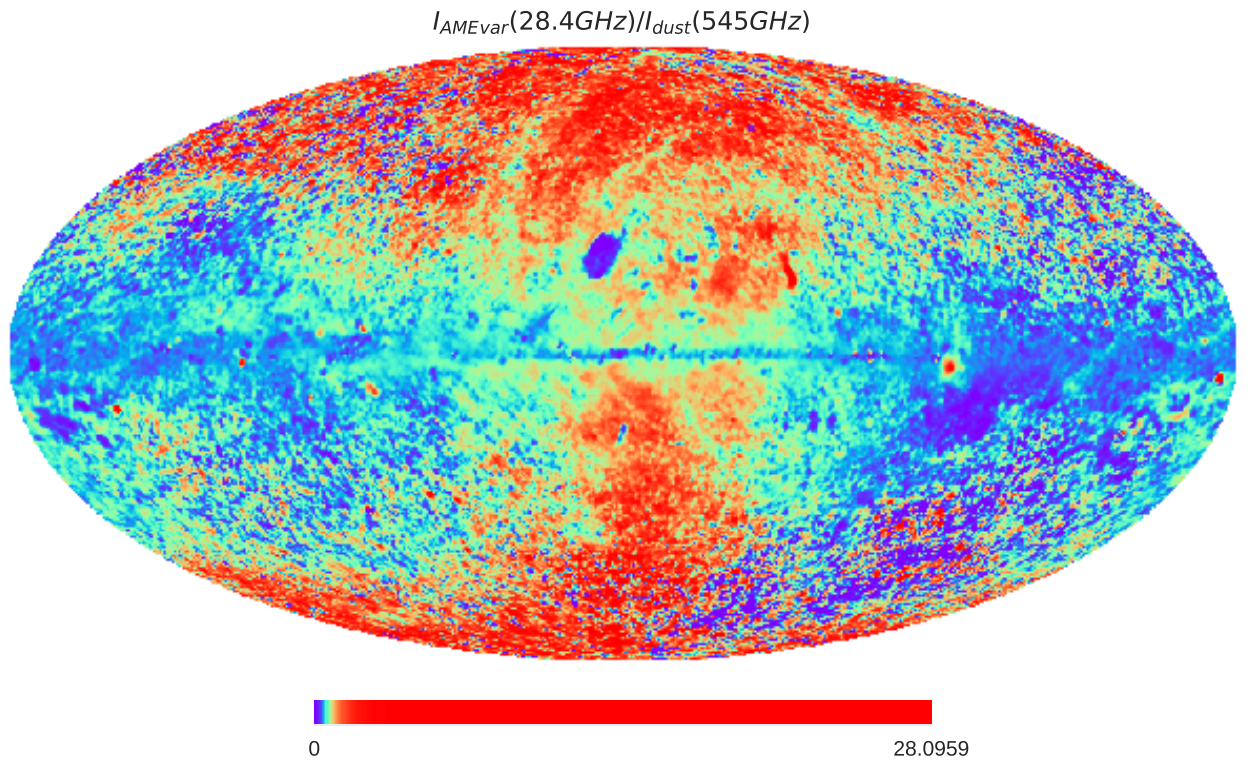


Figure 2.6: All-sky map of the ratio of two COMMANDER components- the frequency-varying AME component divided by the intensity of thermal dust emission at 545 GHz.

---

## 446 Free-free emission

447 Unlike the PCSync component, the fitting of the Planck COMMANDER free-free component map  
 448 (hereafter, PCff) does not employ any free-free dominated emisison map.<sup>7</sup>.

### 449 2.3.2 Thermal dust emission

450 “Thermal dust emission” in the COMMANDER context refers to dust emission in the Rayleigh Jeans-  
 451 regime, as the COMMANDER fitting does not include photometric constraints on the thermal emis-  
 452 sion peak, or consider small grain emission on the Wiens side.

### 453 2.3.3 COMMANDER-AME: Peak Frequency Distribution

454  $I_{AME}\nu_{var}$  In addition, there is an “AME component map”, which presumes that AME originates from  
 455 spinning dust. While acknowledging that such a decomposition lacks a physical justfication, Planck  
 456 Collaboration et al. (2016b) break the AME into two components: a spatially varying peak frequency  
 457 component, and a spatially constant peak frequency component. However as seen in Fig. 2.7, virtually  
 458 all of the fitted peak frequncies for  $AME_{var}$  beyond the reach of WMAP and Planck. Only the fitted  
 459 global frequency, 33.5 GHz for the spatially constant component, is covered.

460 The COMMANDER maps give each component’s intensity at a different “reference frequency”  
 461 (corresponding to photometric bands). In other words, the COMMANDER AME intensities are not  
 462 peak intensities. Moreover they are intensities calculated for a single template spinning dust spectrum.  
 463 Instead of parameterizing the spinning dust physical conditions, they apply a frequency shift and  
 464 amplotide shift to a spectrum corresponding to a warm neutral phase of the ISM. This modeling  
 465 approach was applied first in the WMAP spinning dust analysis, and was later adopted by the Planck  
 466 Collaboration to investigate AME-prominent regions (Planck Collaboration et al. 2014d). Fig. 2.9  
 467 demonstrates such shifted templates. Without fitting the “spdust” model parameters, the for a common  
 468 “reference intensity” at a common “reference frequency”.

469 For these reasons, we are very cautious in deriving conclusions from comparisons with the COM-  
 470 MANDE AME map. The authors themselves include a similar disclaimer. However since there is  
 471 currently no better all-sky component separation available, we carry out our investigation with this  
 472 dataset. Improving on the COMMANDER AME map would be extremely difficult without lower

---

<sup>7</sup>The Planck AME paper, Planck Collaboration et al. (2014d), had employed the H- $\alpha$  map by Reynolds et al. (1998)

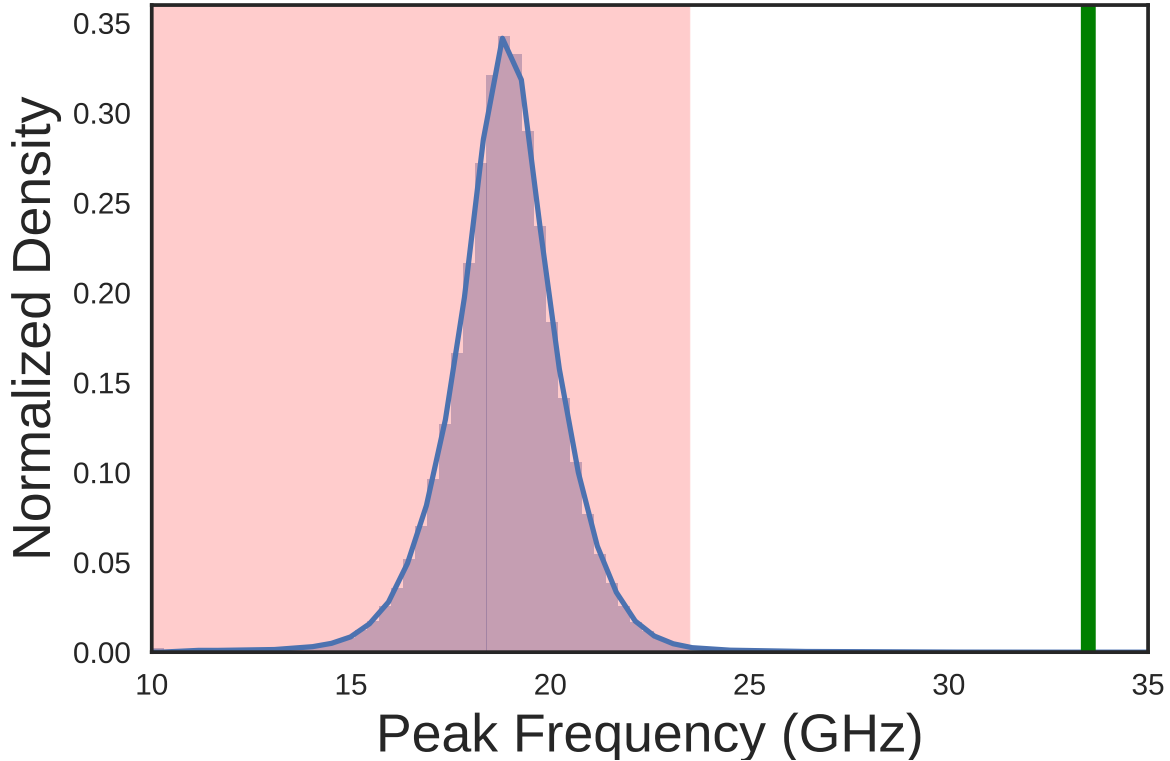


Figure 2.7: The peak frequencies of the varying component  $AME_{var}$ . The pink shaded region indicates frequencies not covered by either WMAP or Planck. The green line at 33.5 GHz indicates the peak frequency of  $AME_{fix}$ .

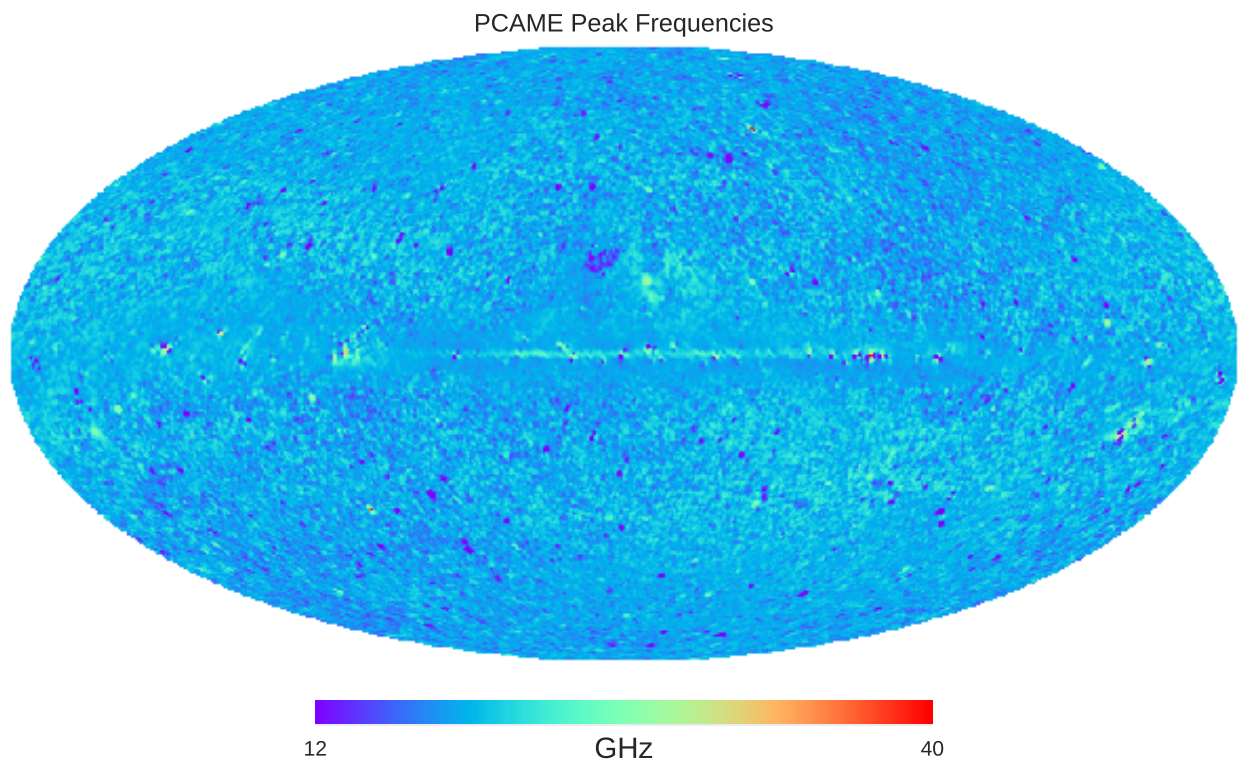


Figure 2.8: All-sky map of the peak frequencies of the varying component  $AME_{var}$ , corresponding to Fig. 2.7.

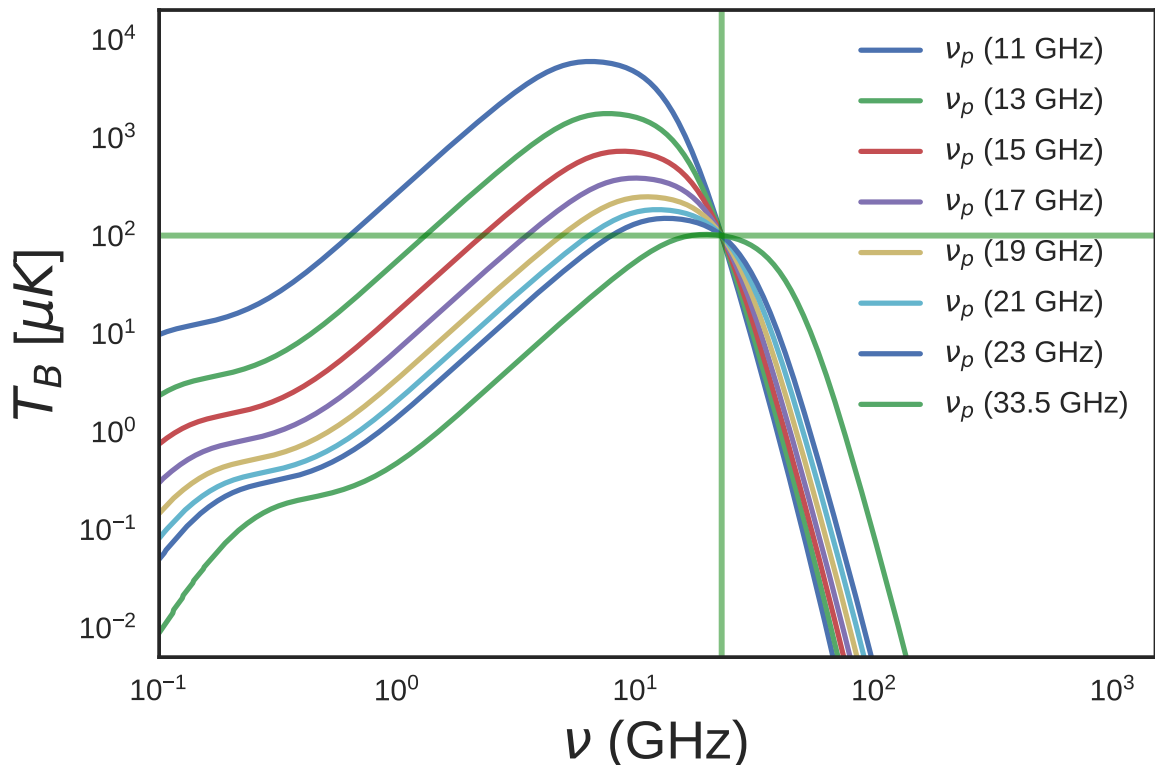


Figure 2.9: Spdust template spinning dust profiles fitted by PC15X when calculating  $AME_{var}$ . The reference frequency, 22.8 GHz is indicated by the vertical green line. Each template has the same  $AME_{var}$  amplitude of  $100 \mu\text{K}$ , indicated by the horizontal green line, plotted to highlight the potential deviation between  $AME_{var}$  and the actual peak intensity.

473 frequency constraints and/or higher resolution observations of not only the AME itself but the contri-  
 474 bution from synchrotron and free-free emisson.

## 475 2.4 All-sky Data Processing

476 The HFI, FIS, and IRIS maps used here are downloaded from their respective online repositories, as  
 477 all-sky HEALPix<sup>8</sup> maps (Górski et al. 2005). NSIDE 2048 maps. In the case of the IRC maps, we first  
 478 create HEALPix maps from the 4,857 all-sky survey tiles using the Aladin all-sky data visualization  
 479 platform (Bonnarel et al. 2000). NSIDE 2048 implies an average pixel spacing of  $1.7'$ . The maps  
 480 are then degraded to NSIDE 1024 before carrying out a Gaussian-beam smoothing to a  $1^\circ$  FWHM.  
 481 Map smoothing itself is done in spherical harmonic space, before the maps and transformed back to  
 482 position space. These steps are handled by the smoothing function contained in the healpy python  
 483 package. Following the smoothing process, the maps are degraded once more to NSIDE 256, or  $15'$   
 484 pixel-width<sup>9</sup>. The value of each of the larger NSIDE 256 pixels, comes from the mean of its parent  
 485 NSIDE 1024 pixels. The purpose of this processing is to ensure that all of the maps have the same  
 486 resolution as the PR2 AME map.

---

<sup>8</sup>HEALPix core software is described at <http://healpix.sourceforge.net>. The HEALPix python package “healpy” used in this work is available at: <https://github.com/healpy/healpy>

<sup>9</sup>HEALPix pixel scale rebinning carried out with healpy.ud\_grade

<sup>487</sup>

# Chapter 3

<sup>488</sup>

## All-sky Analysis

<sup>489</sup> We first would like to note that “all-sky analysis” can be a bit misleading. The term tends to lead  
<sup>490</sup> readers to the idea of a definitive study

<sup>491</sup> We will first introduce our all-sky analysis of the AME vs. IR emission. This approach relies on  
<sup>492</sup> HEALPix maps smoothed to  $1^\circ$  angular resolution. We start with an all-sky AME to IR comparison,  
<sup>493</sup> looking for global patterns among all pixels (except those within  $10^\circ$  of the ecliptic plane.)

<sup>494</sup>

### 3.1 All-sky Pixel Domain Analysis

<sup>495</sup>

#### 3.1.1 All-sky cross correlations

<sup>496</sup> In order to look more closely how the the AME to IR relationship varies with wavelength, we first  
<sup>497</sup> do a simple cross-correlation test. Figure 3.4 shows Spearman’s  $\rho$  ( $r_S$ ) , for each of the 12 bands  
<sup>498</sup> sampled.Throughout this work we adopt  $r_s$  as our statistical metric. Rather than the linearity of  
<sup>499</sup> potential IR-MW relationships, we are primarily interested in the extent of monotonic relatedness.

<sup>500</sup>

#### 3.1.2 Pixel mask

<sup>501</sup> **Zodical light** To keep our analysis comparable to previous works, we exclude pixels within  $10^\circ$  of  
<sup>502</sup> the ecliptic plane. Even though we use the Zodi-subtracted maps ((Kelsall et al. 1998; Kondo et al.  
<sup>503</sup> 2016)), the Zodi residuals are still problematic (especially in the MIR.) Espeically at high ecliptic lat-  
<sup>504</sup> itudes, the relative uncertainty of the Zodi-level is not well estimated; S/N may significantly reduced  
<sup>505</sup> in for faint pixels, mainly for the 9 through 25  $\mu\text{m}$ .

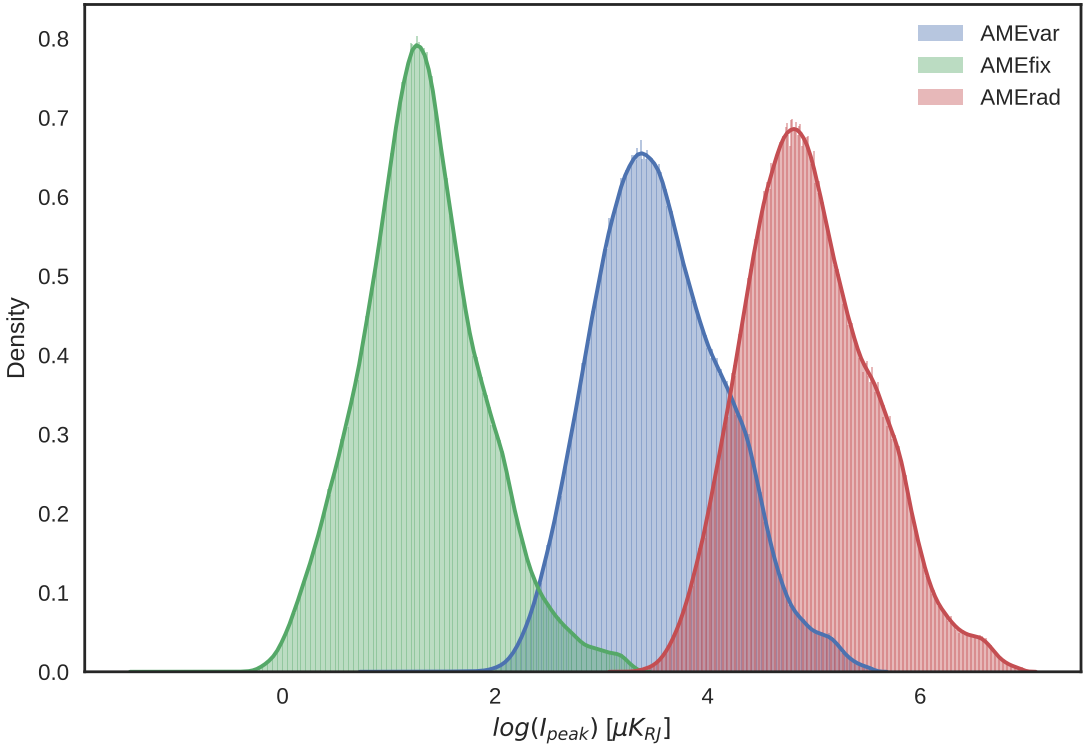


Figure 3.1: Histograms of the peak intensity AME maps calculated from the original COMMANDER-AME reference frequency maps. AMEvar (blue) indicates the distribution of all pixels in the map, with intensities calculated at their peak frequencies (see Fig.

2.7). AMEfix gives the peak intensity of the spatially-constant frequency component.

### 3.1.3 AME data

The AME data comes from the PR2 astrophysical component datasets, as described in Ch. 2. We show the comparison for 3 different AME estimates: the two AME components ( $AME_{var}$  and  $AME_{fix}$ ) as they are provided in PR2 (intensities quoted at reference frequencies<sup>1</sup>). The  $AME_{fix}$  peak freq. is spatially constant at 33.5 GHz, with  $AME_{var}$  and  $AME_{fix}$  calculated at each pixel's peak frequency rather than the PR2 reference freq. We do this because there is nothing physically special about the Planck reference frequencies, and because the PR2  $AME_{var}$  component intensity could vary significantly from the intensity at the peak of the fitted spinning dust template. Thirdly we show the corr-correlation matrix with a single AME metric- calculating the integrated intensity at each pixel, for both AME components, creating an  $AME_{sum}$  component. Fig. 3.1 compares the distribution of these 3 components.

Figure 3.3 visualizes the cross-correlation matrix for each of the IR bands. The AME does not

<sup>1</sup>22.8 GHz for  $AME_{var}$ , 41 GHz for  $AME_{fix}$

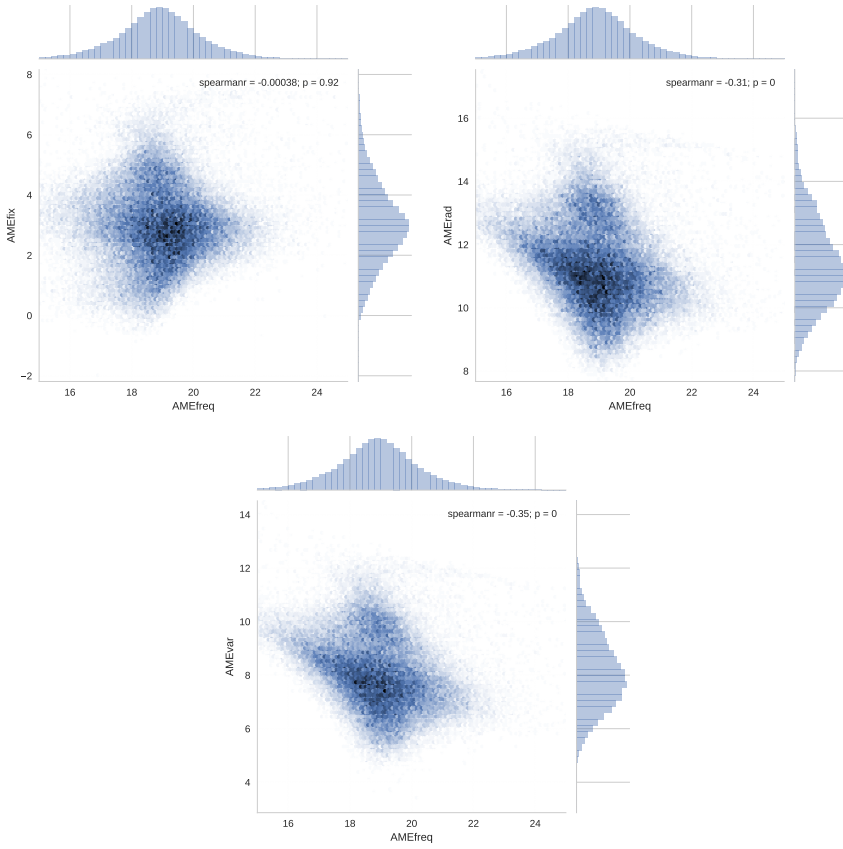


Figure 3.2: AME intensities vs. peak frequencies..

518 show a strong correlation with other bands at  $|l| > 10$ . At  $|l| < 10$ , the FIR bands show stronger  
 519 correlation. The PAH-tracing bands show a stronger correlation than bands at 18 to 60  $\mu\text{m}$ , but  
 520 weaker than AME vs. the FIR bands.

## 521 3.2 Spatial variation of correlations

522 To understand how these trends may vary across the sky, we produce an all-sky maps of  $r_s$  for AME  
 523 vs. IR emission. From the NSIDE 256 input maps of AME and 4 IR wavelength maps, we produce  
 524 NSIDE 8 maps of  $r_s$ . These maps are shown in Fig. 3.6.

## 525 3.3 Discussion

### 526 3.3.1 AME:Dust

527 As noted in Ch. 1, previous studies found that the AME generally correlates at dust-related IR wave-  
 528 lengths (Ysard et al. 2010; Planck Collaboration et al. 2014d; Hensley et al. 2016). We see the same  
 529 overall pattern in the present study.

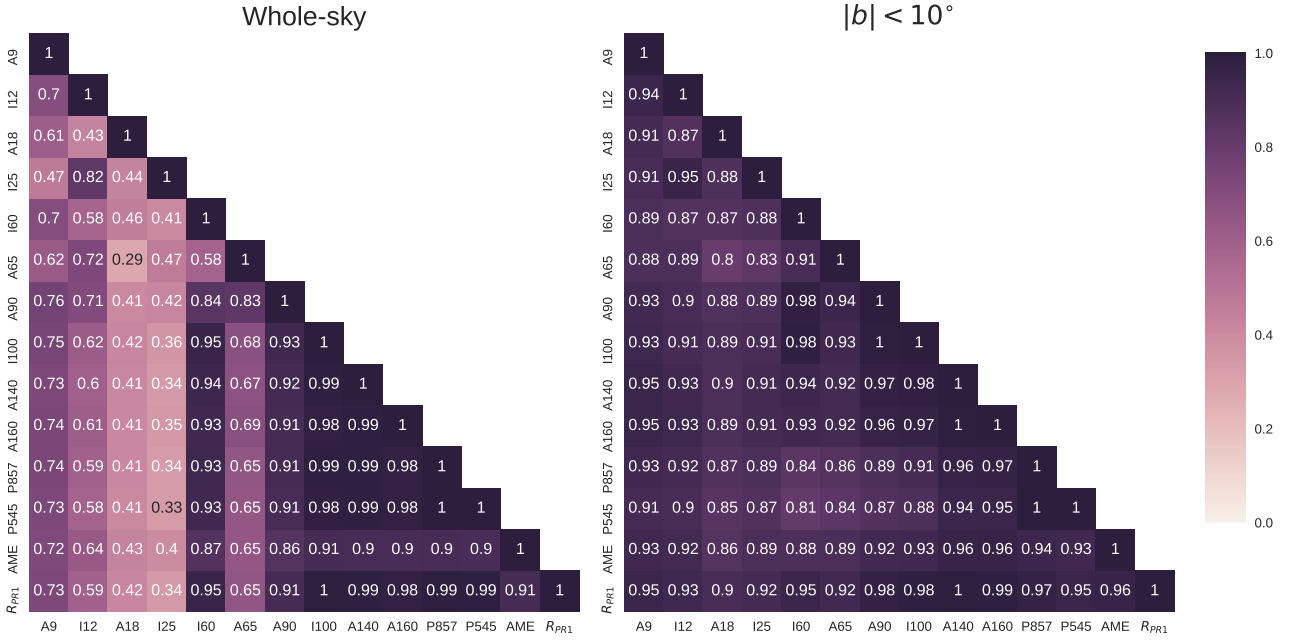


Figure 3.3: ALL-SKY cross-correlation matrix for the 12 infrared bands sampled, and the AME map. The color-scale indicates  $(r_S)$ . Results are based on the full sky (excluding pixels within  $10^\circ$  of the ecliptic plane).

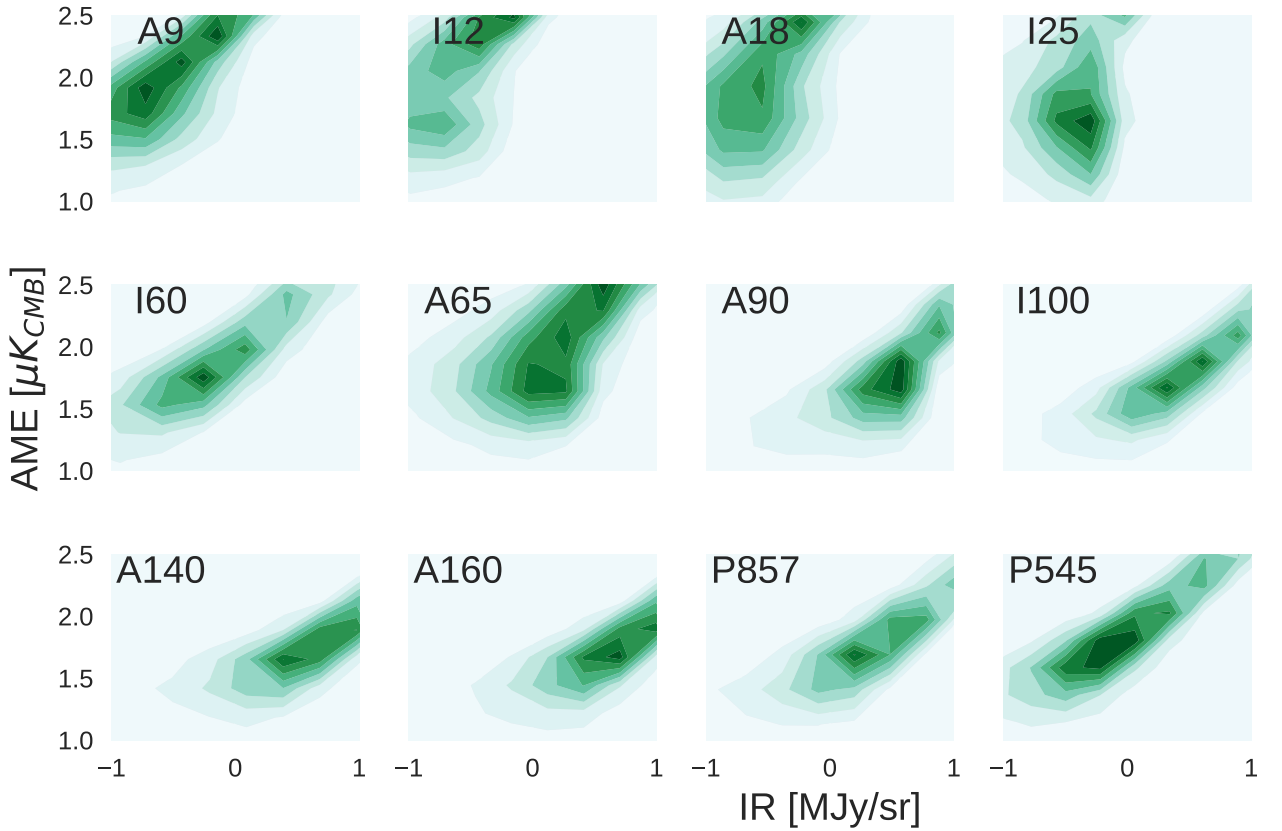


Figure 3.4: ALL-SKY kernel density estimates of 12-band infrared photometry against the PR2 AME map. Pixels within  $10^\circ$  of the ecliptic plane are excluded. 'A' indicates AKARI; 'D', DIRBE; 'I', IRAS, and 'P' Planck. The number after each letter indicates the band central nominal wavelength in microns (or frequency in GHz, in the case of the Planck bands.)

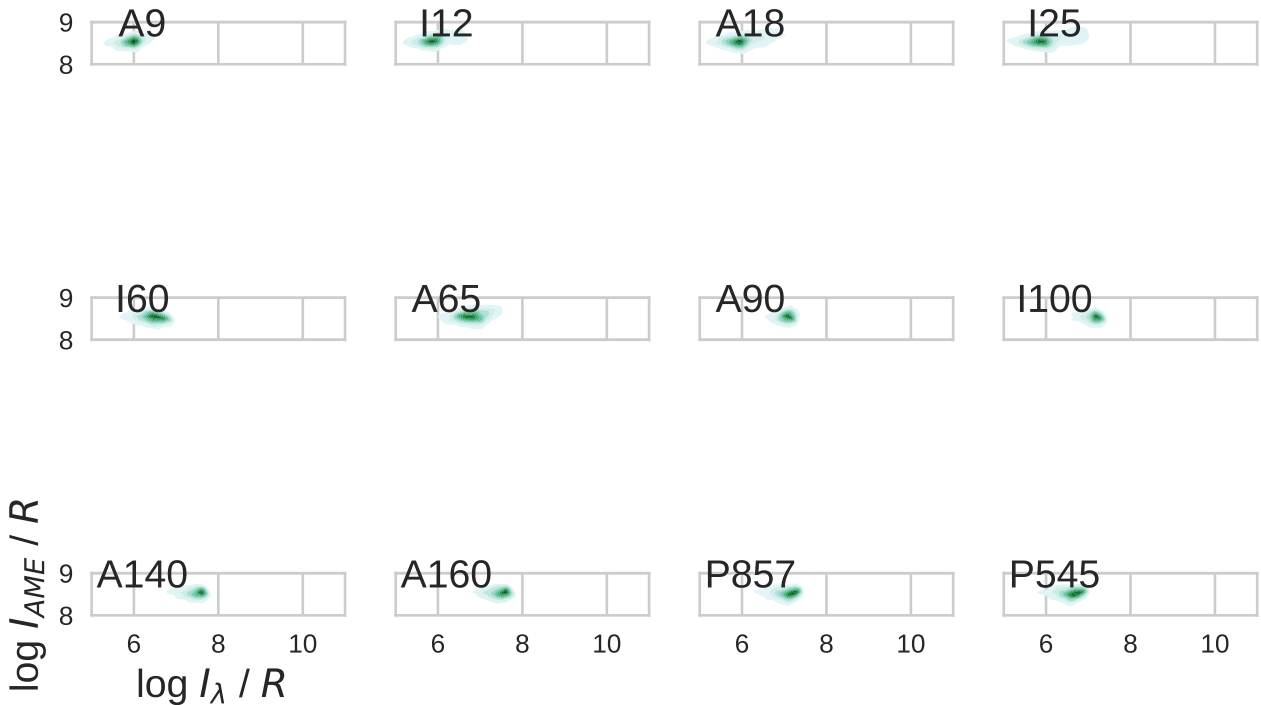


Figure 3.5: Similar comparison to Fig. 3.4, with both the IR and the AME intensities scaled by the PR2 dust radiance ( $R$ ) for each pixel.

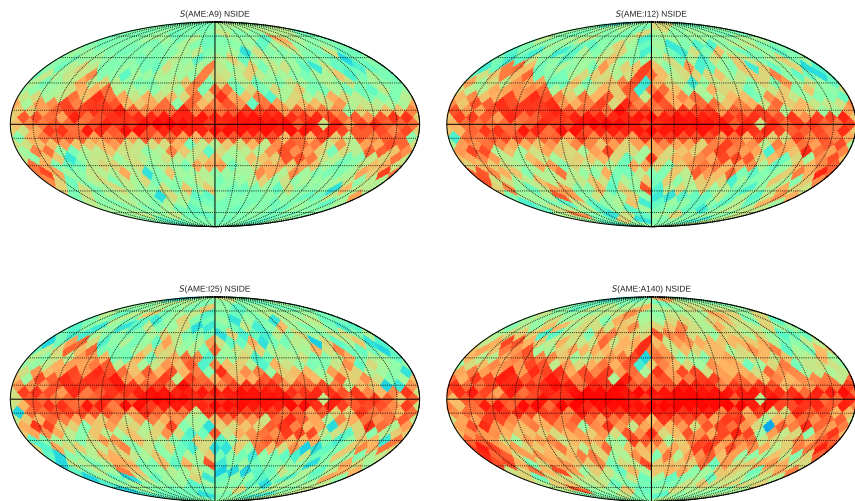


Figure 3.6: Spatial map of  $r_s$  between the AME and IR intensity for 4 bands:  $9 \mu\text{m}$ ,  $12 \mu\text{m}$ ,  $25 \mu\text{m}$ , and  $140 \mu\text{m}$ .  $r_s$  is calculated for all NSIDE 256 pixels within each NSIDE 8 pixel-sized bin.

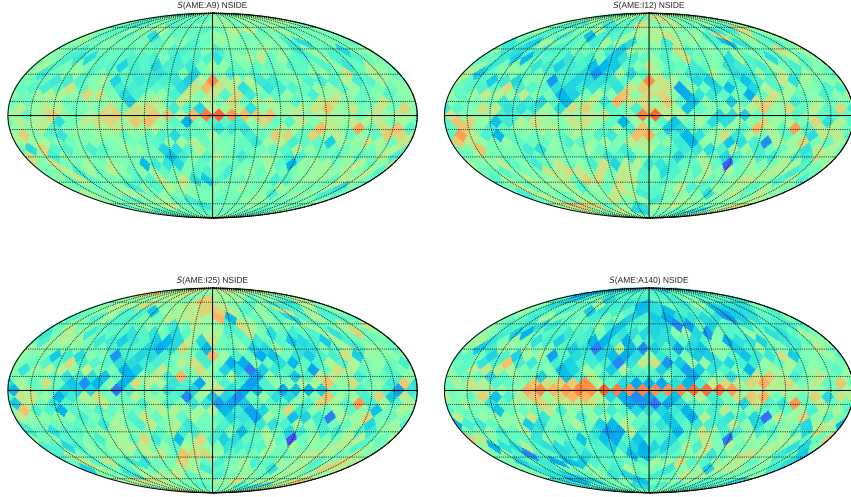


Figure 3.7: Spatial map of  $r_s$  between the AME and IR intensity as in Fig. 3.6, but with the AME and IR maps first normalized by dust radiance  $R$ .

530 In our all-sky comparison, we find a first-order correlation between IR intensity and AME inten-  
 531 sity, for each of the 12 wavelengths sampled. This is again consistent with the previous investiga-  
 532 tions of the AME cited above, in that the FIR emission shows the tightest correlation with the AME inten-  
 533 sity.

534 In testing for a second-order correlation, we divided the IR intensities and AME intensity by  
 535 the dust radiance, and again performed the band-by-band all-sky comparison. There is evidence of  
 536 a residual correlation between  $I_{MIR}$  and  $I_{AME}/R$ . Unsurprisingly, the strong correlation between  
 537  $I_{FIR}$  and  $I_{AME}$  disappears when scaling by  $R$ , as the FIR bands are dominated by thermal dust  
 538 emission. In this case, we again find no evidence of an improved correlation for the PAH-dominated  
 539 bands.

540 The closeness of the correlation coefficients found here is consistent with the results of the IRAS  
 541 vs. AME correlation test result from Planck Collaboration et al. (2014d). They found that the corre-  
 542 lation coefficient among the 4 IRAS bands (12, 25, 60, and 100  $\mu\text{m}$ ) differ from one another only by  
 543 about 5%, across the whole set of 98 regions. The trend of AKARI MIR and FIR data vs. the AME  
 544 does not disagree with their IRAS comparison. This work adds that bands longer than IRAS 100  $\mu\text{m}$   
 545 also correlate strongly with AME, especially the two Planck/HFI bands used.

### 546 3.3.2 AME:PAH

547 Each of the bands sampled show correlation with the AME, however the FIR bands always show the  
 548 strongest correlation. In fact, the correlation pattern of AME vs. each of the IR bands, very strongly

549 resembles the correlation results of the Planck HFI bands vs. all of the other bands (Fig. 3.3.) This  
550 is readily apparent from the pixel-density plots in Fig. 3.4, wherein the FIR bands pixels show a very  
551 similar density profile vs. the AME. In attempting to factor out this first-order correlation, dividing  
552 the AME and IR intensities by the dust radiance for each pixel, we find the there is still a residual  
553 correlation between the MIR bands and the AME. The FIR bands scaled by the dust radiance, as  
554 expected, lack correlation with  $I_{AME}/R$ .

555 **3.3.3 AME: $T, G_0$**

556 According to spinning dust theory outlined in Draine & Lazarian (1998a) and in subsequent works by  
557 Ysard & Verstraete (2010), the AME profile and intensity will depend in part on the ISRF- but as is  
558 well-stated in Hensley & Draine (2017a), exactly how the ISRF will affect the AME SED is a more  
559 complicated question. Absorbed starlight photons may be able to rotationally excite the carriers, but  
560 if an enhanced ISRF leads to increased dust heating, then the increased IR emission can rotationally  
561 de-excite the carriers. However the ISRF affects not only the dust temperature but ionization of the  
562 carriers.

563 Hensley et al. (2016) looked at the  $AME/R$  ratio vs.  $T$  and found only a slight anti-correlation of  
564  $P = -0.06$ .

565 **3.3.4 Microwave foreground component separation**

566 There are known degeneracies between the foreground parameters of the COMMANDER maps  
567 (spinning-dust, and free-free, synchrotron components as described in Planck Collaboration et al.  
568 (2016b).) This can be demonstrated by comparing the ratio map of the PCXV intensity to thermal  
569 dust intensity.

# <sup>570</sup> Chapter 4

## <sup>571</sup> Analysis of an interesting AME region: <sup>572</sup> $\lambda$ Orionis

### <sup>573</sup> 4.1 An interesting AME region

<sup>574</sup> The  $\lambda$  Orionis molecular ring, also known as the Meissa Ring is a massive stucture surrounding the  
<sup>575</sup>  $\lambda$  Orionis O-type star. The ring contains an HII region, ionized by LOrí itself and its OB associates  
<sup>576</sup> (Murdin & Penston 1977). What had been thought of as a starforming region of missing molecular  
<sup>577</sup> gas. At the time Murdin & Penston (1977) even speculated that this could be evidence of an alternate  
<sup>578</sup> starformation pathway, writing: “Notably we need to know if  $\lambda$ Ori is an example of a different mode  
<sup>579</sup> of star formation or [...] simply a case in which the progenitor molecular cloud was exhausted within  
<sup>580</sup> the last one or two million years.”

<sup>581</sup> Maddalena (1986); Maddalena & Morris (1987). (and references therein) noted a ring of material  
<sup>582</sup> likely being pushed out by the central, historically well-known  $\lambda$  Orionis Association of B-type stars  
<sup>583</sup> and surrounding HII reigon.

#### <sup>584</sup> 4.1.1 Where does the ring come from?

<sup>585</sup> Cunha & Smith (1996) argued that the ring may have resulted from a supernova explosion, further  
<sup>586</sup> speculating that LOrí may have been a companion of the progenitor.  $\lambda$  Orionis is a known binary  
<sup>587</sup> system, however its current companion is the a B-type star. (Murdin & Penston 1977) . The central  
<sup>588</sup> region is heated by the  $\lambda$  Orionis star itself, and the Orion OB association it belongs to (Ochsendorf  
<sup>589</sup> et al. 2015). The region is known to host several young stellar and protostellar objects (Koenig et al.

590 2015).

591 At approx.  $10^\circ$  wide, we can see the outline of the structure even in the low ( $1^\circ$  FWHM) resolution  
592 PCAME map. The ring shape itself is thought to originate from a supernova, or perhaps combined  
593 effects of the entire star formation history of the  $\lambda$  Orionis Association, including the formation of its  
594 surrounding HII region (Aran 2009).

### 595 4.1.2 A well-studied region

596 Although the  $\lambda$  Orionis region has been a popular target for study since approximately the 1980s. Duerr  
597 et al. (1982) wrote of the relative lack of work on the overall region: “Surprisingly, this interesting  
598 complex has been little studied”. While this seems surprising given the number of works on the region  
599 in the literature now, it is really the advent of all-sky missions that have driven more recent interest.  
600 The large angular size is such that all-sky surveys were a natural boon for study of such extended  
601 structures. WISE especially was a huge source of insight (Koenig et al. 2015). More recently, Planck  
602 Collaboration et al. (2016c) strongly highlighted the region as a strong candidate for further AME  
603 investigation.

## 604 4.2 Investigative approach

605 We have carried out an initial comparison of the AME of this region with its mid to far-IR dust  
606 emission. The region is shown in Fig. 4.1 as it appears in  $1^\circ$ -smoothed A9 data Images at each  
607 wavelength used here are included as in appendix to this thesis. The ring structure itself indicates  
608 excess microwave emission attributed to AME (white contours) while the central region is dominated  
609 by free-free emission (Aran 2009; Koenig et al. 2015). Free-free emission coming from the Hii phase  
610 surrounding the  $\lambda$  Orionis association dominates the region’s morphology in LFI images. (Planck  
611 Collaboration et al. 2016c). Taking the hint from Planck Collaboration et al. (2016c) that this may  
612 be among the more reliably component separated regions, we evaluate if there is any preferential  
613 relationship between any parameter of dust emission and the AME.

## 614 4.2.1 Data preparation

615 As indicated in Ch. 2, we use 12 photometric all-sky maps. For the IRC data (A9 and A18), we  
 616 produce mosaics of  $\lambda$  Orionis from the individual tiles provided in the internal all-sky archive.<sup>1</sup> For  
 617 the other sources, HEALPix all-sky maps are available publicly, at sufficient resolution relative to  
 618 their native resolutions.<sup>2<sup>34</sup></sup>

## 619 4.2.2 Extraction from HEALPix maps

620 For the data obtained via HEALPix maps, we employ the “healpix2wcs” functionality provided in the  
 621 “gnomdrizz” python package<sup>56</sup> A9 and A18 images are produced by regridding the images with the  
 622 “montage” software by NASA/IPAC. All of the images for all of the bands are based on a common  
 623 FITS header which has a pixel grid spacing equal to the average pixel width in the NSIDE 256  
 624 HEALPix scheme. A background estimation and subtraction is made

## 625 4.2.3 Multi-wavelength characterization

626 Figure 4.2 shows the region in 12 photometric bands, from the mid to far IR. Contours indicate the  
 627 region’s shape in the PCAME map. Figure 4.3 shows IR to AME cross correlation plots, for all pixels  
 628 within the  $10^\circ$  by  $10^\circ$   $\lambda$  Orionis region. The correlation is most clear for the shortest and for the  
 629 longest wavelength bands, and weakens the most at around  $60\ \mu\text{m}$ . The weakening of the correlation  
 630 score appears to come from brighter 25 to  $90\ \mu\text{m}$  emission within the ring. The spectrum is consistent  
 631 with warm thermal dust emission, heated by  $\lambda$  Orionis and its associates. The ring structure itself  
 632 appears relatively consistent across all bands. Fig.

## 633 4.2.4 Ionization fraction

634 We attempt to estimate the relative fraction of charged to neutral PAHs via the  $R(A9 : I12)$  band  
 635 ratio. A9 is known to cover ionized PAH features (as well as neutral) whereas I12 primarily covers  
 636 neutral features.

---

<sup>1</sup>IRC all-sky data is still in the proprietary phase at the time of this writing, but should be public by April 2018.

<sup>2</sup>Planck data was retrieved from the NASA IPAC online archive at [http://irsa.ipac.caltech.edu/data/Planck/release\\_2/all-sky-maps/](http://irsa.ipac.caltech.edu/data/Planck/release_2/all-sky-maps/)

<sup>3</sup>AKARI/FIS data

<sup>4</sup>IRAS/IRIS data

<sup>5</sup>Available at <http://cade.irap.omp.eu/dokuwiki/doku.php?id=software>

<sup>6</sup>“drizzlib” 1.2.2 and earlier were not able to correctly access HEALPix files with multiple fields/columns. See appendix for our recommended workaround.

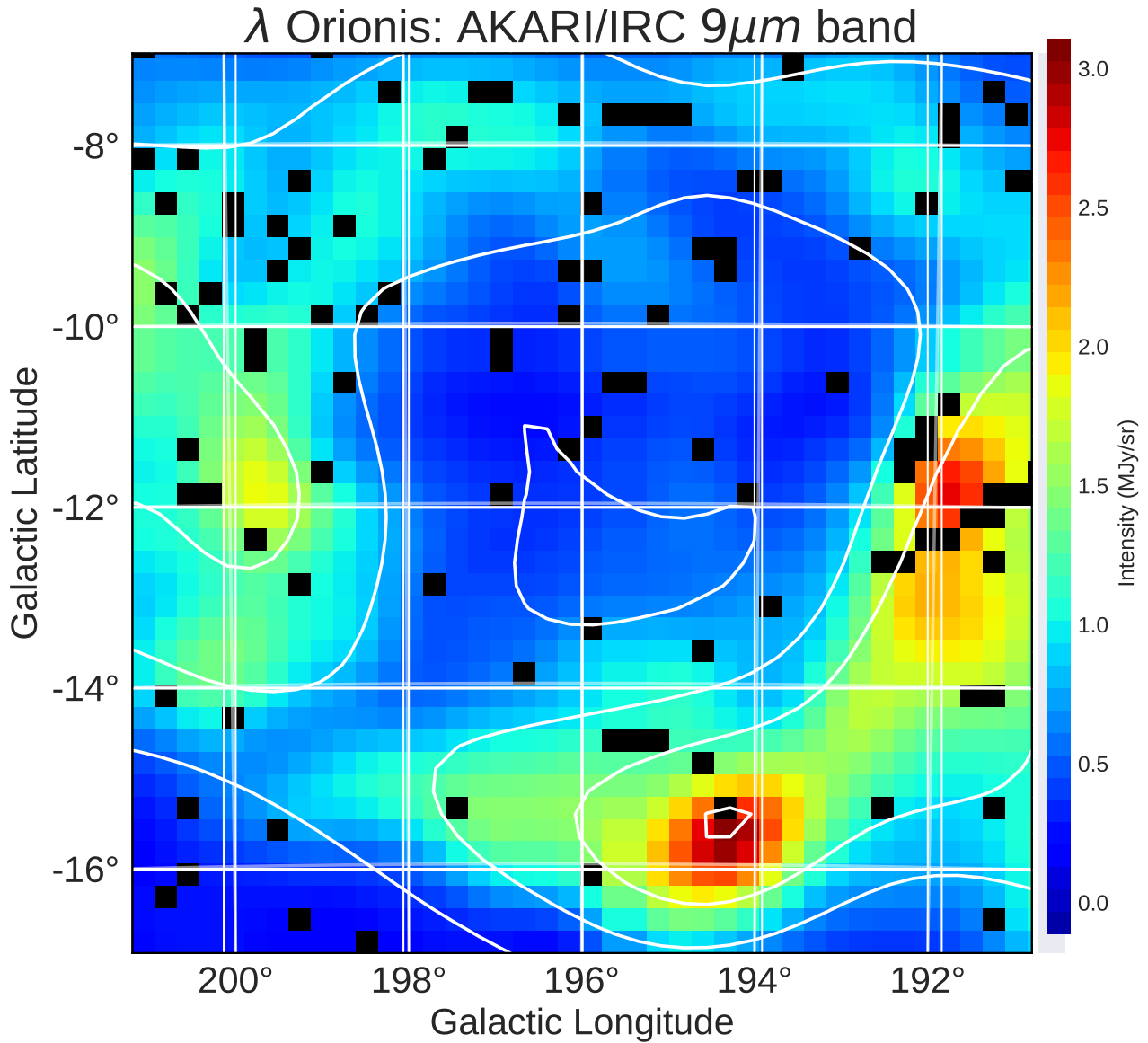


Figure 4.1:  $\lambda$  Orionis as it appears in the AKARI 9  $\mu$ m data. Contours indicate the AME, as given by the Planck PR2 AME map. The image is smoothed to a 1° PSF (much larger than the original 10 arcsec map). The  $\lambda$  Orionis star itself is approximately located at the center of the image.

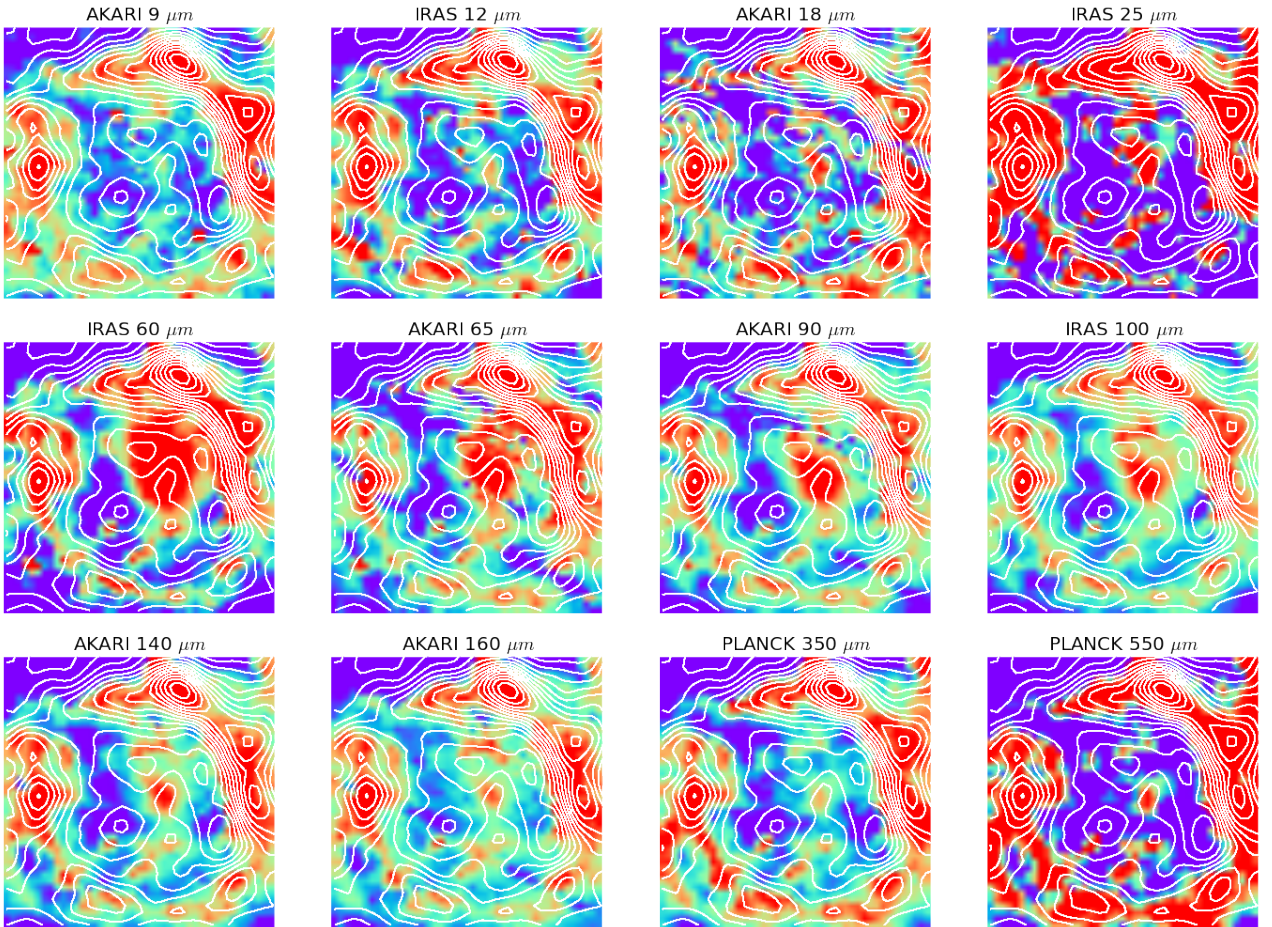


Figure 4.2: A grid of thumbnails showing the  $\lambda$  Orionis region's structure, at 12 wavelengths, along with AME contours (shown in white countours). Spatial correlation seems to be the best at the shortest and longest wavelengths (AKARI/IRC 9  $\mu m$  and Planck/HFI 550  $\mu m$ ). The images are smoothed and interpolated for demonstration. Figure 4.1 demonstrates the actual pixel grid used for the SED fitting and intensity correlation tests.

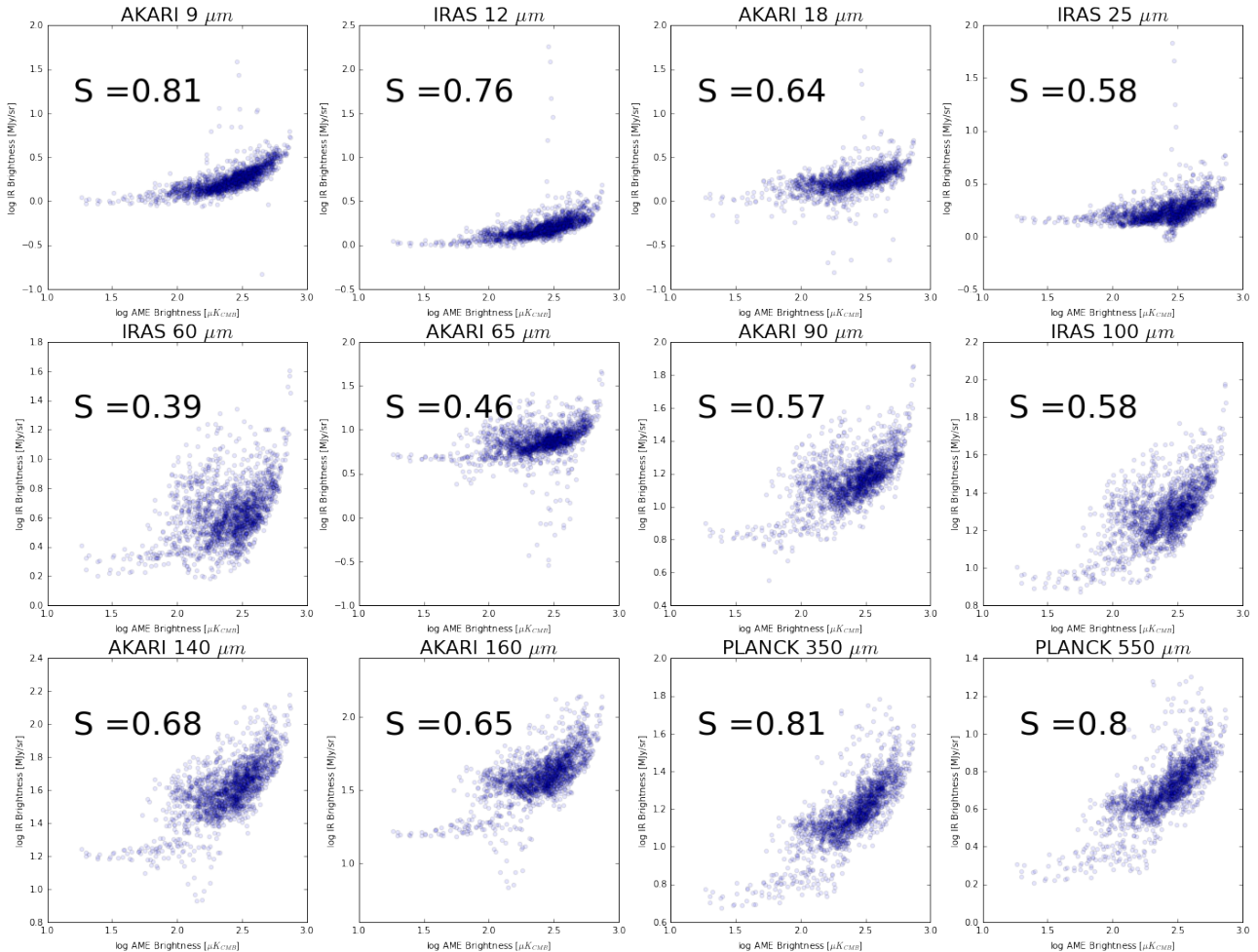


Figure 4.3: Pixel cross-correlation for all pixels in the  $\lambda$  Orionis cut-out region.  $r_s$  indicates the Spearman rank correlation coefficient for each plot.

	A9	1	0.93	0.94	0.84	0.75	0.78	0.64	0.66	0.72	0.85	0.84	0.92	0.9	0.89	0.58
D12	0.93	1	0.97	0.83	0.84	0.83	0.76	0.74	0.81	0.91	0.89	0.93	0.91	0.84	0.6	
I12	0.94	0.97	1	0.84	0.82	0.85	0.78	0.77	0.84	0.93	0.92	0.93	0.91	0.85	0.62	
A18	0.84	0.83	0.84	1	0.89	0.91	0.68	0.57	0.67	0.77	0.75	0.72	0.69	0.61	0.39	
D25	0.75	0.84	0.82	0.89	1	0.97	0.77	0.58	0.7	0.77	0.76	0.69	0.66	0.56	0.41	
I25	0.78	0.83	0.85	0.91	0.97	1	0.79	0.62	0.73	0.8	0.79	0.7	0.66	0.58	0.43	
D60	0.64	0.76	0.78	0.68	0.77	0.79	1	0.88	0.94	0.86	0.86	0.67	0.61	0.48	0.57	
A65	0.66	0.74	0.77	0.57	0.58	0.62	0.88	1	0.96	0.9	0.88	0.76	0.7	0.58	0.62	
A90	0.72	0.81	0.84	0.67	0.7	0.73	0.94	0.96	1	0.94	0.93	0.8	0.75	0.63	0.65	
A140	0.85	0.91	0.93	0.77	0.77	0.8	0.86	0.9	0.94	1	0.99	0.91	0.86	0.75	0.63	
A160	0.84	0.89	0.92	0.75	0.76	0.79	0.86	0.88	0.93	0.99	1	0.89	0.85	0.73	0.63	
P857	0.92	0.93	0.93	0.72	0.69	0.7	0.67	0.76	0.8	0.91	0.89	1	0.99	0.89	0.62	
P545	0.9	0.91	0.91	0.69	0.66	0.66	0.61	0.7	0.75	0.86	0.85	0.99	1	0.89	0.59	
AMEfix	0.89	0.84	0.85	0.61	0.56	0.58	0.48	0.58	0.63	0.75	0.73	0.89	0.89	1	0.63	
AMEvvar	0.58	0.6	0.62	0.39	0.41	0.43	0.57	0.62	0.65	0.63	0.63	0.62	0.59	0.63	1	
	A9	D12	I12	A18	D25	I25	D60	A65	A90	A140	A160	P857	P545	AMEvar	AMEfix	

Figure 4.4:  $r_s$  correlation matrix for all of the data used in the  $\lambda$  Orionis analysis.

### 637 4.2.5 SED Fitting

638 We performed a full dust SED fitting on the LOri photometry, according to the Galliano et al. (2011)  
639 dust model. We used a mixture of amorphous carbon and silicate dust. Indeed, this dust mixture is  
640 more emissive than the standard silicate-graphite (Draine & Li 2007), by a factor of 2-3. As was  
641 shown by Herschel, in the LMC (Galliano et al. 2011), and by Planck, in the Milky Way (Planck  
642 Collaboration et al. 2016d), this increase of emissivity is necessary to have a proper fit of the sub-mm  
643 emission. We assume that the radiation field heating this dust mixture is the Galactic ISRF (Mathis  
644 et al. 1983), scaled by a factor  $U$ . We also assume, following Dale et al. (2001), that the dust is  
645 exposed to a distribution of starlight intensity, distributed as:

$$dM_{dust} \propto U^{-\alpha} dU \quad (4.2.1)$$

646 between  $U_{min}$  and  $U_{max}$ , where  $U_{min}$ ,  $U_{max}$  and  $\alpha$  are free parameters. An old stellar population  
647 template (PEGASE; (Fioc & Rocca-Volmerange 1997)) is added to this SED in order to model the  
648 near-IR emission. We perform a simple least-squares analysis.

## 649 4.3 Discussion

### 650 4.3.1 AME:PAH

651 In  $\lambda$  Orionis we found that across the whole region, AKARI 9  $\mu\text{m}$  emission and Planck 545 GHz  
652 emission were the most strongly correlated with AME, having Spearman coefficients of 0.81 and 0.80.  
653 The results may be consistent with a scenario in which PAH mass, cold dust, and the AME are all  
654 tightly correlated. Weaker correlation from 25 to 70  $\mu\text{m}$  may indicate that AME is weaker in regions  
655 of warmer dust and stronger radiation fields. This would be consistent with PCXV wherein highly  
656 significant AME regions tended to have a lower dust temperature than other regions. The fact that the  
657 correlation strengths of PAH-tracing mission the FIR emission are similar is in-line with what we have  
658 seen in Ysard et al. (2010) and Hensley et al. (2016). In those works, the two relationships (MIR vs.  
659 AME and FIR vs. AME) are very close, although these two papers are odds as to which relationship is  
660 stronger, and thus in their final interpretation. However in the investigation of the Perseus molecular  
661 cloud complex by Tibbs et al. (2011), PAH emission (as well as VSG emission and hydrogen column  
662 density,  $N_H$ ) does not show a strong correlation with AME compared to environmental parameters,

---

663 such as dust temperature.

# 664 Chapter 5

## 665 Summary

666 From these results, we cannot confirm or rule out a spinning-PAH hypothesis on an all-sky,  $1^\circ$  scale.  
667 While nanosilicates or magnetic dipole emission from dust may be plausible contributors to the AME,  
668 as shown in Hoang et al. (2016); Hensley & Draine (2017a), we do not find (at least at resolutions  
669 considered here) that PAHs can be ruled-out as a carrier. While it is true that the FIR in our study has  
670 a tighter correlation with AME than PAH-related bands, the correlation with PAH emission remains.  
671 This is true both when considering AME intensity to either this is a coincidental correlation- PAHs  
672 and AME are both correlated with the “actual” carrier/s of AME, MIR photometric bands are not as  
673 good of a tracer of the actual PAH mass as we believed, or perhaps that PAHs are indeed contributing  
674 to the AME but that they are just one of multiple sources of the AME.

675 If it can be shown that IR emission from non-PAH small dust particles, such as nanosilicates  
676 strongly correlates with the AME, another very interesting question would need to be addressed:  
677 why does PAH emission *not* show a strong correlation? Do PAHs not have the range of dipole  
678 moments needed to produce emission in the 10 - 90 GHz range? Because, as is described in Draine  
679 & Lazarian (1998a) and again in Hensley & Draine (2017b), such small particles should be spinning  
680 at the frequencies consistent with AME. Thus if we believe a particular class of small dust particles  
681 to exist, PAHs, nanosilicates, or otherwise- then they must be producing microwave emission, unless  
682 they do not have a permanent electric dipole.

683 If there is a sufficient abundance of PAHs with an electric dipole, then we must consider the pos-  
684 sibility that the data currently available to do not offer the necessary spatial resolution, or that the  
685 photometric bands used do not allow us to adequately separate the individual dust components (i.e.  
686 the PAH features from potential nanosilicate features) and/or microwave foreground emission com-  
687 ponents (free-free from spinning-dust.) We look forward to continued environment-resolved compar-

---

688 ions to investigate the potential AME-PAH (or AME-nanosilicates, iron nanoparticles) relationship  
689 in a region by region, especially given the disagreement we find between our examination of lambda  
690 Orionis and the all-sky analysis.

691 This project is supported by JSPS and CNRS under the Japan–France Research Cooperative Pro-  
692 gram. We would like to give special thanks to the AME Workshop 2016 attendees and organizer,  
693 Chris Tibbs, for enlightening discussions. Thanks also to Nathalie Ysard and Steven Gibson, and the  
694 staff of Grid, Inc. for helpful feedback.

# <sup>695</sup> A Note on Data Dimensionality

<sup>696</sup> While we aim to demonstrate the application of high dimensionality in these studies, we do not wish  
<sup>697</sup> to mislead readers that we have assembled a 12-dimensional photometric dataset, simply because we  
<sup>698</sup> have 12 wavebands. This statement may seem nonsensical at first, but makes sense when we consider  
<sup>699</sup> the covariance of the data. Just from the outside, and our faithful belief that FIR dust emission looks  
<sup>700</sup> something like a blackbody, or modified blackbody, or at the very least we can agree that emission  
<sup>701</sup> from dust in thermal equilibrium would produce some sort of peaked continuum emission spanning  
<sup>702</sup> multiple photometric bands' width. If we agree on this point, then it follows naturally that said bands  
<sup>703</sup> would be highly correlated with one another. This means that the number of truly independent data  
<sup>704</sup> dimensions is not only lower than the number of bands used here, it is much lower.

<sup>705</sup> Fig. 1 shows the % of variance in the data retained by the first  $n$  principal components. Principal  
<sup>706</sup> components are found essentially by first finding the covariance matrix of the input data, and then  
<sup>707</sup> diagonalizing this matrix- the eigenvectors will be the basis vectors of each principal component. The  
<sup>708</sup> eigenvalues will give the explained covariance per component. Applied in this manner, the compo-  
<sup>709</sup> nents may not necessarily have a clear physical interpretation, but from a data analytics perspective  
<sup>710</sup> we can at least assess the redundancies in our data. Thus from Fig. 1, and choosing an arbitrary  
<sup>711</sup> covariance "acceptable loss" of 99%, our photometric data set steeply reduces to 3 dimensions. The  
<sup>712</sup> first component contains 98% of the total variance.

---

How many useful components are in our data?

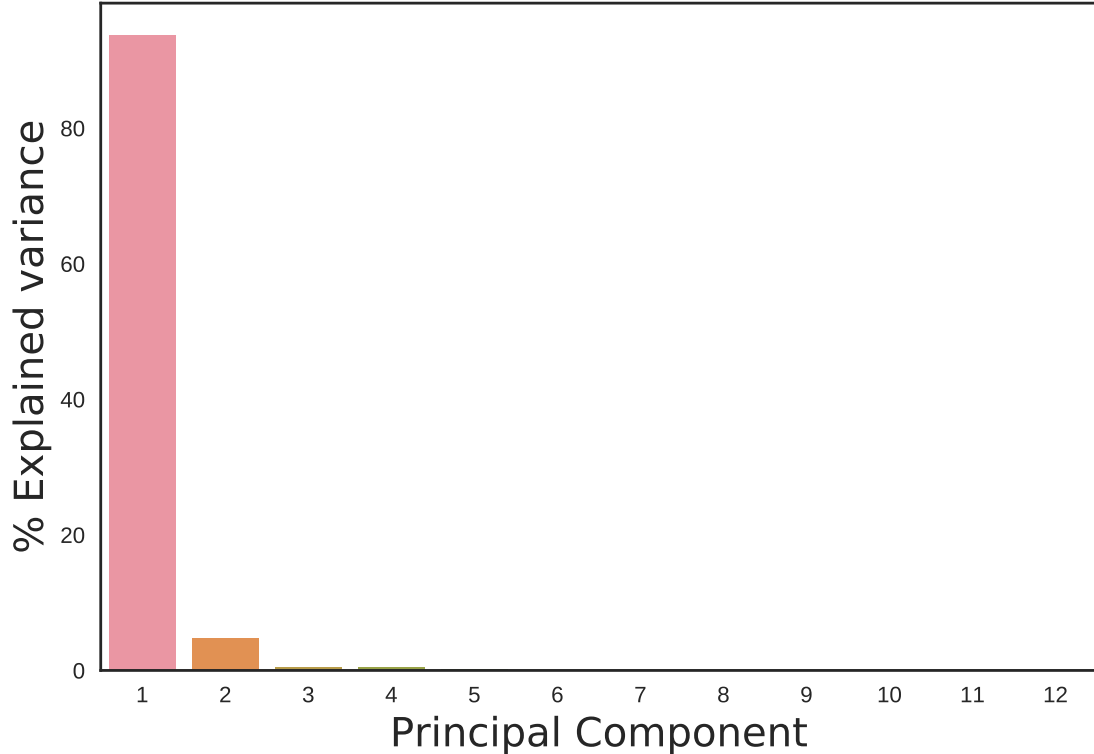


Figure 1: Explained variance decline for principal component analysis performed on a set of 12 all-sky infrared maps. The first three components account for over 99% of the total variance. The PCA fit is performed on the whole sky, after whitening the data, using the “scikitlearn” library.

713 This research made use of Montage. It is funded by the National Science Foundation under Grant  
714 Number ACI-1440620, and was previously funded by the National Aeronautics and Space Admin-  
715 istration's Earth Science Technology Office, Computation Technologies Project, under Cooperative  
716 Agreement Number NCC5-626 between NASA and the California Institute of Technology

# 717 References

- 718 Ali-Haimoud, Y. 2010, SpDust/SpDust.2: Code to Calculate Spinning Dust Spectra, Astrophysics Source Code  
719 Library
- 720 Ali-Haïmoud, Y. 2014, MNRAS, 437, 2728
- 721 Ali-Haïmoud, Y., Hirata, C. M., & Dickinson, C. 2009, MNRAS, 395, 1055
- 722 AMI Consortium et al. 2012, MNRAS, 423, 1463
- 723 Andrews, H., Boersma, C., Werner, M. W., Livingston, J., Allamandola, L. J., & Tielens, A. G. G. M. 2015,  
724 ApJ, 807, 99
- 725 Aran, A. B. 2009, PhD thesis, UNIVERSIDAD AUTONOMA DE MADRID
- 726 BICEP2 Collaboration et al. 2014, Physical Review Letters, 112, 241101
- 727 Bonnarel, F., et al. 2000, A&AS, 143, 33
- 728 Compiègne, M., et al. 2011, A&A, 525, A103
- 729 Cunha, K., & Smith, V. V. 1996, A&A, 309, 892
- 730 Dale, D. A., Helou, G., Contursi, A., Silbermann, N. A., & Kolhatkar, S. 2001, ApJ, 549, 215
- 731 de Oliveira-Costa, A., Kogut, A., Devlin, M. J., Netterfield, C. B., Page, L. A., & Wollack, E. J. 1997, ApJ,  
732 482, L17
- 733 de Oliveira-Costa, A., et al. 2002, ApJ, 567, 363
- 734 Dickinson, C., Paladini, R., & Verstraete, L. 2013, Advances in Astronomy, 2013, 1
- 735 Doi, Y., et al. 2015, PASJ, 67, 50
- 736 Draine, B. T. 2011, Physics of the Interstellar and Intergalactic Medium
- 737 Draine, B. T., & Hensley, B. 2013, ApJ, 765, 159
- 738 Draine, B. T., & Lazarian, A. 1998a, ApJ, 494, L19
- 739 —. 1998b, ApJ, 508, 157
- 740 —. 1999, ApJ, 512, 740
- 741 Draine, B. T., & Li, A. 2001, ApJ, 551, 807
- 742 —. 2007, ApJ, 657, 810
- 743 Duerr, R., Imhoff, C. L., & Lada, C. J. 1982, ApJ, 261, 135
- 744 Dwek, E. 1986, ApJ, 302, 363
- 745 Erickson, W. C. 1957, ApJ, 126, 480

---

*REFERENCES*

- 746 Ferrara, A., & Dettmar, R.-J. 1994, *ApJ*, 427, 155
- 747 Finkbeiner, D. P., Schlegel, D. J., Frank, C., & Heiles, C. 2002, *ApJ*, 566, 898
- 748 Fioc, M., & Rocca-Volmerange, B. 1997, *A&A*, 326, 950
- 749 Flauger, R., Hill, J. C., & Spergel, D. N. 2014, *J. Cosmology Astropart. Phys.*, 8, 039
- 750 Galliano, F., et al. 2011, *A&A*, 536, A88
- 751 Giard, M., Lamarre, J. M., Pajot, F., & Serra, G. 1994, *A&A*, 286
- 752 Górski, K. M., Hivon, E., Banday, A. J., Wandelt, B. D., Hansen, F. K., Reinecke, M., & Bartelmann, M. 2005,  
753 *ApJ*, 622, 759
- 754 Hanson, D., et al. 2013, *Physical Review Letters*, 111, 141301
- 755 Haslam, C. G. T., Salter, C. J., Stoffel, H., & Wilson, W. E. 1982, *A&AS*, 47, 1
- 756 Hensley, B. S., & Draine, B. T. 2017a, *ApJ*, 836, 179
- 757 —. 2017b, *ApJ*, 834, 134
- 758 Hensley, B. S., Draine, B. T., & Meisner, A. M. 2016, *The Astrophysical Journal*, 827, 45
- 759 Hoang, T., Draine, B. T., & Lazarian, A. 2010, *ApJ*, 715, 1462
- 760 Hoang, T., Vinh, N.-A., & Quynh Lan, N. 2016, *ApJ*, 824, 18
- 761 Hoyle, F., & Wickramasinghe, N. C. 1970, *Nature*, 227, 473
- 762 Ishihara, D., et al. 2010, *A&A*, 514, A1
- 763 Johnson, H. L. 1966, *ARA&A*, 4, 193
- 764 Jones, A. P. 2009, *A&A*, 506, 797
- 765 Kawada, M., et al. 2007a, *PASJ*, 59, 389
- 766 —. 2007b, *PASJ*, 59, S389
- 767 Kelsall, T., et al. 1998, *ApJ*, 508, 44
- 768 Koenig, X., Hillenbrand, L. A., Padgett, D. L., & DeFelippis, D. 2015, *AJ*, 150, 100
- 769 Kogut, A., Banday, A. J., Bennett, C. L., Gorski, K. M., Hinshaw, G., & Reach, W. T. 1996, *ApJ*, 460, 1
- 770 Kondo, T., et al. 2016, *AJ*, 151, 71
- 771 Leitch, E. M. 1998, PhD thesis, CALIFORNIA INSTITUTE OF TECHNOLOGY
- 772 Li, A., & Draine, B. T. 2001, *ApJ*, 554, 778
- 773 Lovas, F. J., McMahon, R. J., Grabow, J.-U., Schnell, M., Mack, J., Scott, L. T., & Kuczkowski, R. L. 2005,  
774 *Journal of the American Chemical Society*, 127, 4345, pMID: 15783216
- 775 Maddalena, R. J. 1986, PhD thesis, National Aeronautics and Space Administration. Goddard Inst. for Space  
776 Studies, New York, NY.
- 777 Maddalena, R. J., & Morris, M. 1987, *ApJ*, 323, 179
- 778 Mathis, J. S., Mezger, P. G., & Panagia, N. 1983, *A&A*, 128, 212

- 779 Miville-Deschénes, M.-A., & Lagache, G. 2005, ApJS, 157, 302
- 780 Murakami, H., et al. 2007, PASJ, 59, 369
- 781 Murdin, P., & Penston, M. V. 1977, MNRAS, 181, 657
- 782 Neugebauer, G., et al. 1984, ApJ, 278, L1
- 783 Ochsendorf, B. B., Brown, A. G. A., Bally, J., & Tielens, A. G. G. M. 2015, ApJ, 808, 111
- 784 Onaka, T. 2000, Advances in Space Research, 25, 2167
- 785 Onaka, T., Yamamura, I., Tanabe, T., Roellig, T. L., & Yuen, L. 1996, PASJ, 48, L59
- 786 Onaka, T., et al. 2007, PASJ, 59, 401
- 787 Penzias, A. A., & Wilson, R. W. 1965, ApJ, 142, 419
- 788 Perrott, Y. C., et al. 2018, MNRAS, 473, 1157
- 789 Pettit, E., & Nicholson, S. B. 1922, ApJ, 56, 295
- 790 —. 1928, ApJ, 68
- 791 Planck Collaboration et al. 2011a, A&A, 536, A1
- 792 —. 2011b, A&A, 536, A20
- 793 —. 2014a, A&A, 571, A1
- 794 —. 2014b, A&A, 571, A8
- 795 —. 2014c, A&A, 571, A12
- 796 —. 2014d, A&A, 565, A103
- 797 —. 2016a, A&A, 594, A1
- 798 —. 2016b, A&A, 594, A10
- 799 —. 2016c, A&A, 594, A25
- 800 —. 2016d, A&A, 586, A132
- 801 —. 2017, A&A, 599, A51
- 802 Purcell, E. M. 1976, ApJ, 206, 685
- 803 Reynolds, R. J., Tufte, S. L., Haffner, L. M., Jaehnig, K., & Percival, J. W. 1998, PASA, 15, 14
- 804 Sellgren, K. 1984, ApJ, 277, 623
- 805 Sheehy, C., & Slosar, A. 2017, ArXiv e-prints
- 806 Takita, S., et al. 2015, PASJ, 67, 51
- 807 Thorwirth, S., Theulé, P., Gottlieb, C. A., McCarthy, M. C., & Thaddeus, P. 2007, ApJ, 662, 1309
- 808 Tibbs, C. T., et al. 2011, MNRAS, 418, 1889
- 809 von Hausegger, S., & Liu, H. 2015, J. Cosmology Astropart. Phys., 8, 029
- 810 Young, E. T., et al. 2012, ApJ, 749, L17
- 811 Ysard, N., Juvela, M., & Verstraete, L. 2011, A&A, 535, A89
- 812 Ysard, N., Miville-Deschénes, M. A., & Verstraete, L. 2010, A&A, 509, L1
- 813 Ysard, N., & Verstraete, L. 2010, A&A, 509, A12